Available online at www.sciencedirect.com
ScienceDirect
Journal of Sound and Vibration 308 (2007) 164–189
JOURNAL OF SOUND AND VIBRATION
www.elsevier.com/locate/jsvi

Two-dimensional sublamination theory for analysis of functionally graded plates

P. Frank Pai[a,*], Anthony N. Palazotto[b]

[a]Department of Mechanical and Aerospace Engineering, University of Missouri-Columbia, Columbia, MO 65211, USA
[b]Department of Aeronautics and Astronautics, Air Force Institute of Technology, Wright-Patterson Air Force Base, OH 45433, USA

Received 11 April 2006; received in revised form 19 January 2007; accepted 18 July 2007
Available online 4 September 2007

Abstract

Presented is a two-dimensional sublamination theory for analysis of plates made of functionally graded materials. The sublamination plate theory extends a layer-wise higher-order shear-deformation theory for laminated plates by considering material properties being continuous functions of the thickness coordinate and using a new concept of sublamination to increase the degrees of freedom. The theory accommodates free shear stress conditions on the bonding surfaces, accounts for non-uniform deformation-dependent distributions of transverse shear stresses through the thickness, can be used for evaluating boundary restraint effects, and can be used for analyzing thin and thick plates with any boundary conditions. A sublamination plate element based on this theory is developed and validated for static and dynamic analysis. The degrees of freedom of the element is adaptable. For an element away from boundaries, it's degrees of freedom can be reduced at the elemental level without loss of accuracy. Analytical shear warping functions are presented. Moreover, modal analysis of functionally graded plates with different boundary conditions is performed to show the capability and accuracy of the theory.

1. Introduction

Some structural components serve under conditions that require material properties vary within the component. For example, a kitchen knife is required to be hard at its cutting edge and strong and tough elsewhere. A gear needs to have a hard, wear-resistant surface but a tough body. A turbine blade needs to have a strong, tough and creep-resistant body but a refractory and oxidation-resistant outer surface. A composite made of ceramic on one side and metal on the other side is ideal for wear-resistant linings in the mineral processing industry; the hard ceramic face is for the exposed side and the tough metal face is for the rear side that is bolted or welded to a support frame. Other examples include the heat shield of rockets and human implants (e.g., bone and dental implants), which demands a heat or corrosion resistant outer layer and a tough metallic base material in order to increase the life time of the component. Composite materials manufactured by traditional methods may fulfill such requirements, but a traditional composite is a man-made geometrical

*Corresponding author.
E-mail address: paip@missouri.edu (P. Frank Pai).

0022-460X/$ - see front matter © 2007 Published by Elsevier Ltd.
doi:10.1016/j.jsv.2007.07.027

combination of different pre-existing phases and is a compromise between the properties of the component materials. Unfortunately, abrupt transition in material composition and properties within a conventional composite component often results in severe local stress concentration due to manufacturing (i.e., residual stresses) or external mechanical/thermal loading. For a composite structure formed by mixing different materials, temperature changes during fabrication and subsequent service can generate high internal stresses and/or unwanted pre-curvatures as a result of unequal thermal expansion/contraction between the constituent phases. Similarly, different local deformation fields are induced in the two materials during imposed mechanical loading because of their different mechanical properties. This incompatibility in thermomechanical deformation results in internal stresses and strains that play a key role in the creation of threading dislocations, localized yielding around interfaces, interfacial debonding, microcracking and brittle failure of the hard phase, or separation by void nucleation and growth in the ductile phase. Hence, composite materials with smooth gradation of material properties had been occasionally suggested in the literature [1], and those were the precursors of functionally graded materials (FGMs). However, as a formulated concept studied under a large organized research program, the term FGM originated in Japan in 1984 during a spaceplane project that required a thermal barrier material capable of withstanding a surface temperature of 2000 K in an oxidizing environment and a temperature gradient of 1000 K across a thickness less than 10 mm and being tough and thermally conductive on the lower-temperature side [2].

A functionally graded material is a composite material whose composition and microstructure are locally varied during manufacturing so that certain variations of local material (thermal and mechanical) properties are achieved. An FGM is very often a two-component composite characterized by a compositional gradient from one component to the other, and hence the properties of both components can be fully utilized. One important group of low-cost FGMs is ceramic–metal FGMs. The smooth gradation of material composition from ceramic to metal would enhance the toughness of the ceramic face and also provide a ceramic–metal bonding better than that produced by sintering a ceramic and then coating it with metal. FGMs are ideal candidates for applications involving severe thermal gradients, including thermal structures in advanced aircraft and aerospace engines and computer circuit boards. Comparing to traditional composites merits of FGMs include: (1) small thermal stresses and a designed peak thermal stress location; (2) small stress concentrations at material interfaces in an FGM; (3) strong interfacial bonding; (4) reduced free-edge effects; (5) delayed plastic yielding; and (6) increased fracture toughness by reducing driving force for crack growth along/across material interfaces [3,4].

A functionally graded material can be manufactured by chemical or physical vapor deposition methods, plasma spraying methods, powder metallurgy methods, self-propagating high-temperature combustion synthesis methods, surface chemical reaction methods, sintering methods, and many other techniques [2,3]. A common approach toward the fabrication of an FGM is to vary material composition through the thickness of a thin substrate. However, if the manufacturing facility is versatile enough, gradient material composition along two dimensions is possible. The concept of FGMs allows full integration of material fabrication and structural engineering into the final design of structural components. Because the static and dynamic behavior of an FG structure is determined by the mechanical and thermal properties of the FGM and the actual boundary conditions and mechanical/thermal loads, structural analysis and design of material fabrication process need to be performed before actual manufacturing of the FGM, and it is a multi-disciplinary task and a reverse engineering problem. Because of the variation of material composition, many problems exist, including design of fabrication process in order to have an FGM with desired material properties, manufacturing-induced residual stresses, difficulties in material property characterization, negative effects of stress concentrations at free surfaces and edges, and difficulties in the modelling and analysis of structures made of FGMs. Research areas related to FGMs include process metallurgy, composite synthesis, mechanics and micromechanics of composites, fracture mechanics, and design methodologies. The science and technology of FGMs has been dramatically advanced during the last decade. Comprehensive reviews of current FGM research can be found in Refs. [2–5].

To extend conventional structural analysis techniques for functionally graded structures certain advances in macrostructural property characterization and thermomechanical modelling are needed. Because of non-uniform material distribution, design of functionally graded structures faces challenging modelling and analysis problems that exist in traditional composite structures. Thermomechanical analysis and engineering

of functionally graded structures require effective properties of each FGM made of multiple materials. Hence, accurate estimation of effective properties of FGMs is the key to the eventual success in the design of FGMs. However, because precise information about the size, shape, and distribution of material particles in an FGM is not available and the effective moduli of the graded composite must be evaluated based only on the volume fraction distributions and the approximate shape of the dispersed phase. When particles are small, the material properties P_i of a mixture are difficult to be estimated using the volume fractions V_i [2]. Micromechanics models and analysis methods have been developed by researchers to infer the effective properties of an equivalent macroscopically homogeneous composite material, including the Voigt method (i.e., $P = P_1V_1 + P_2V_2$, an arithmetic average), the Reuss method (i.e., $1/P = V_1/P_1 + V_2/P_2$, a harmonic average), a generalized averaging method ($P = P_1V_1 + P_2V_2 + P_{12}V_1V_2$, where P_{12} depends on P_1, P_2, V_1, V_2, and microstructure-dependent quantities), self-consistent methods [6,7], the Mori–Tanaka method [8], differential schemes, bounding techniques, finite-element unit cell models, and numerical modelling of a bulk FGM with boundary conditions [3,9].

Similar to traditional composite laminates, a functionally graded plate (FGP) may experience severe deformation-dependent transverse shear deformations, free-edge effects, and boundary constraint effects due to non-uniform material distribution and thick thickness. Detailed finite-element analysis using small three-dimensional (3D) solid elements can be used to study such problems, but it is cumbersome and time-consuming. However, some exact 3D elasticity solutions that account for deformation-dependent shears exist in the literature [10–14], but they are all for plates with special boundary conditions, especially simply supported boundary conditions. A 2D plate theory that can treat arbitrary boundary conditions and account for deformation-dependent shear deformations and free-edge and boundary constraint effects does not exist.

This work contributes to the modelling and analysis of FGPs by deriving a 2D sublamination plate theory (SPT) that can account for higher-order deformation-dependent transverse shear deformations and boundary effects caused by free edges and warping restraints at boundaries. A method of computing shear warping functions is derived and numerically demonstrated, and a sublamination plate element (SPE) is also formulated and validated.

2. Sublamination plate theory

An FGP can be fabricated by a stepwise or a continuous grading method. Shear warping functions of an FGP fabricated using a stepwise grading method can be derived by layerwise analysis, and shear warping functions of an FGP fabricated using a continuous grading method can also be derived by layerwise analysis with many assumed layers, as shown next.

2.1. Shear warping functions by layerwise analysis

Fig. 1 shows an FGP fabricated using a stepwise grading method and the xyz coordinate system for modeling, where the xy represents the reference plane of the plate, the x and y are in-plane (or reference plane) coordinates, and the z is the thickness coordinate. To include transverse shear deformations in the modeling of a general FGP, each layer fabricated during one step of the stepwise grading method needs an assumed displacement field because each layer has different material properties. To account for transverse shear stresses, we generalize a layerwise third-order shear-deformation theory [15] by using a new concept of

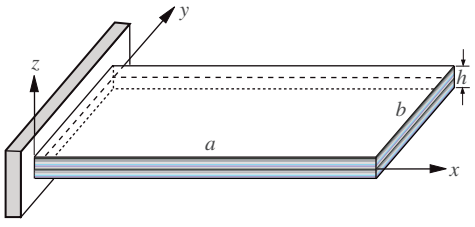

Fig. 1. The plate geometry and the coordinate system.

sublamination to improve the versatility and accuracy in predicting transverse shear stresses and boundary effects. For the ith layer with $z_i \leqslant z \leqslant z_{i+1}$, the displacement field is assumed to be

$$\begin{aligned} u_1^{(i)} &= u - w_x z + \gamma_5^{(i)} z + \alpha_0^{(i)} + \alpha_1^{(i)} z^2 + \alpha_2^{(i)} z^3, \\ u_2^{(i)} &= v - w_y z + \gamma_4^{(i)} z + \beta_0^{(i)} + \beta_1^{(i)} z^2 + \beta_2^{(i)} z^3, \\ u_3^{(i)} &= w, \end{aligned} \tag{1}$$

where $i = 1, \ldots, I$ and I is the total number of layers. Here, $u(x, y, t)$, $v(x, y, t)$, and $w(x, y, t)$ are the displacements of the point on the xy plane (i.e., $z = 0$), t denotes the time, and $\gamma_4^{(i)}$ and $\gamma_5^{(i)}$ are shear rotation angles at the xy plane for the displacement field of the ith layer, as shown in Fig. 2. Moreover, $(\,)_x \equiv \partial(\,)/\partial x$ and $(\,)_y \equiv \partial(\,)/\partial y$. $\alpha_k^{(i)}(x, y, t)$ account for the displacement along the x-direction due to shear warping, $\beta_k^{(i)}(x, y, t)$ account for the displacement along the y-direction due to shear warping, and they are to be determined by the continuity conditions of in-plane displacements and interlaminar shear stresses and the free shear stress conditions on the top and bottom surfaces of the plate as shown next. The transverse normal strain ε_{33} can be accounted for by assuming $u_3^{(i)} = w + \eta_1^{(i)} z + \eta_2^{(i)} z^2$. However, as shown in Ref. [15], ε_{33} is mainly caused by Poisson's effect and the external normal loads on the top and/or bottom surfaces, ε_{33} and the transverse normal stress σ_{33} can be accurately obtained by integrating the 3D equilibrium equations (see Eq. (41b)) after the reference plane deformations u, v, w, $\gamma_4^{(i)}$, and $\gamma_5^{(i)}$ are obtained from a 2D plate theory. Pagano [11] also pointed out that even the classical plate theory can predict σ_{33} well. Because inclusion of ε_{33} and σ_{33} increases the number of dependent variables and formulation and computation difficulties without significant accuracy increase, it is neglected here.

It follows from Eq. (1) that the transverse shear strains of the ith layer are

$$\begin{aligned} \varepsilon_{13}^{(i)} &= \frac{\partial u_1^{(i)}}{\partial z} + \frac{\partial u_3^{(i)}}{\partial x} = \gamma_5^{(i)} + 2z\alpha_1^{(i)} + 3z^2\alpha_2^{(i)}, \\ \varepsilon_{23}^{(i)} &= \frac{\partial u_2^{(i)}}{\partial z} + \frac{\partial u_3^{(i)}}{\partial y} = \gamma_4^{(i)} + 2z\beta_1^{(i)} + 3z^2\beta_2^{(i)}. \end{aligned} \tag{2}$$

The stress–strain relation for the ith layer is given by [16,17]

$$\begin{Bmatrix} \sigma_{23}^{(i)} \\ \sigma_{13}^{(i)} \end{Bmatrix} = [Q_2^{(i)}] \begin{Bmatrix} \varepsilon_{23}^{(i)} \\ \varepsilon_{13}^{(i)} \end{Bmatrix}, \quad [Q_2^{(i)}] = \begin{bmatrix} Q_{44}^{(i)} & Q_{45}^{(i)} \\ Q_{45}^{(i)} & Q_{55}^{(i)} \end{bmatrix},$$

$$Q_{44}^{(i)} = \cos^2\theta G_{23}^{(i)} + \sin^2\theta G_{13}^{(i)}, \quad Q_{55}^{(i)} = \sin^2\theta G_{23}^{(i)} + \cos^2\theta G_{13}^{(i)}, \quad Q_{45}^{(i)} = \sin\theta\cos\theta(G_{13}^{(i)} - G_{23}^{(i)}), \tag{3}$$

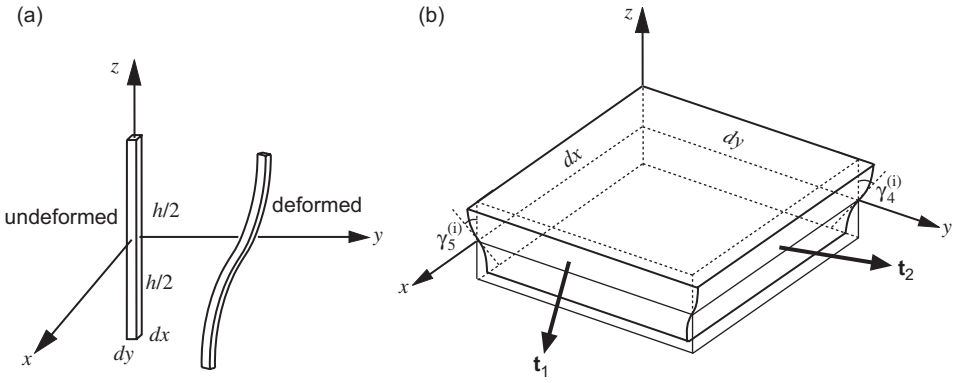

Fig. 2. Shear deformation of a differential plate element: (a) undeformed and deformed configurations, and (b) shear warping of cross sections. The $\mathbf{t}_1$ and $\mathbf{t}_2$ are stress vectors.

where θ is the rotation angle of fibers (if composite laminates) from the material axis $\hat{x}$ to the structural axis x, and $G_{kl}^{(i)}$ are shear moduli. If the ith layer is an isotropic one, $Q_{44}^{(i)} = Q_{55}^{(i)} = G^{(i)}$ and $Q_{45}^{(i)} = 0$.

If there is no delamination, the in-plane displacements u_1 and u_2 and interlaminar shear stresses σ_{13} and σ_{23} are continuous across the interface of any two adjacent layers. Moreover, it is assumed that there is no shear loadings on the top and bottom surfaces of the plate, i.e., $\sigma_{23} = \sigma_{13} = 0$ at $z = z_1$ and $z = z_{I+1}$. Consequently, we have

$$\begin{gathered}
\sigma_{23}^{(I)}(x,y,z_{I+1},t) = 0,\\
\sigma_{13}^{(I)}(x,y,z_{I+1},t) = 0,\\
\sigma_{23}^{(i)}(x,y,z_{i+1},t) - \sigma_{23}^{(i+1)}(x,y,z_{i+1},t) = 0 \quad \text{for } i = 1,\ldots,I-1,\\
\sigma_{13}^{(i)}(x,y,z_{i+1},t) - \sigma_{13}^{(i+1)}(x,y,z_{i+1},t) = 0 \quad \text{for } i = 1,\ldots,I-1,\\
u_2^{(i)}(x,y,z_{i+1},t) - u_2^{(i+1)}(x,y,z_{i+1},t) = 0 \quad \text{for } i = 1,\ldots,I-1,\\
u_1^{(i)}(x,y,z_{i+1},t) - u_1^{(i+1)}(x,y,z_{i+1},t) = 0 \quad \text{for } i = 1,\ldots,I-1,\\
\sigma_{23}^{(1)}(x,y,z_1,t) = 0,\\
\sigma_{13}^{(1)}(x,y,z_1,t) = 0, \alpha_0^{(\hat{i})} = \beta_0^{(\hat{i})} = 0,\\
\alpha_1^{(i)} = \beta_1^{(i)} = 0 \quad \text{for } i = 1,\ldots,I, i \neq \hat{i}.
\end{gathered} \tag{4}$$

The $\hat{i}$th layer is the layer that contains the reference plane xy, and $\alpha_0^{(\hat{i})} = \beta_0^{(\hat{i})} = 0$ for the $\hat{i}$th layer because u and v represent the displacements of the point on the reference plane (see Eq. (1)). These $6I$ algebraic equations can be used to determine the $6I$ unknowns $\alpha_k^{(i)}$ and $\beta_k^{(i)}$ ($k = 0, 1, 2$ and $i = 1,\ldots,I$) in terms of $\gamma_4^{(i)}$ and $\gamma_5^{(i)}$. Substituting Eqs. (1)–(3) into Eq. (4) yields

$$[\overline{A}]\{\alpha\} = [B]\{\gamma\}, \quad \{\alpha\} = [A]\{\gamma\}, \tag{5}$$

where $[\overline{A}]$ is a $6I \times 6I$ constant matrix, $[B]$ is a $6I \times 2I$ constant matrix, $[A]$ $(= [\overline{A}]^{-1}[B])$ is a $6I \times 2I$ constant matrix, and

$$\begin{aligned}
\{\alpha\} &\equiv \{\alpha_0^{(1)}, \alpha_1^{(1)}, \alpha_2^{(1)}, \beta_0^{(1)}, \beta_1^{(1)}, \beta_2^{(1)}, \ldots, \alpha_0^{(I)}, \alpha_1^{(I)}, \alpha_2^{(I)}, \beta_0^{(I)}, \beta_1^{(I)}, \beta_2^{(I)}\}^{\mathrm{T}},\\
\{\gamma\} &\equiv \{\gamma_4^{(1)}, \gamma_5^{(1)}, \ldots, \gamma_4^{(I)}, \gamma_5^{(I)}\}^{\mathrm{T}}.
\end{aligned}$$

To reduce the total number of dependent variables, an FGP of I layers can be grouped into J ($\leqslant I$) sublaminates. If the whole plate is treated as one sublaminate, $\gamma_4 = \gamma_4^{(i)}$ and $\gamma_5 = \gamma_5^{(i)}$ for $i = 1,\ldots,I$. If the first 10 layers is grouped as the first sublaminate, the second 10 layers as the second sublaminate, and the rest as the third sublaminate, we have $\gamma_4^{[2]} = \gamma_4^{(i)}$ and $\gamma_5^{[2]} = \gamma_5^{(i)}$ for $i = 11,\ldots,20$, as shown in Fig. 3. Hence, $[B]$ can be reduced to a $6I \times 2J$ constant matrix, $[A](= [\overline{A}]^{-1}[B])$ is a $6I \times 2J$ constant matrix, and

$$\begin{aligned}
\{\alpha\} &\equiv \{\alpha_0^{(1)}, \alpha_1^{(1)}, \alpha_2^{(1)}, \beta_0^{(1)}, \beta_1^{(1)}, \beta_2^{(1)}, \ldots, \alpha_0^{(I)}, \alpha_1^{(I)}, \alpha_2^{(I)}, \beta_0^{(I)}, \beta_1^{(I)}, \beta_2^{(I)}\}^{\mathrm{T}},\\
\{\gamma\} &\equiv \{\gamma_4^{[1]}, \gamma_5^{[1]}, \ldots, \gamma_4^{[J]}, \gamma_5^{[J]}\}^{\mathrm{T}}.
\end{aligned} \tag{6}$$

With the sublamination shown in Fig. 3 and Eq. (6), one can obtain from the second equation of Eq. (5) that

$$\begin{gathered}
\alpha_0^{(i)} = \sum_{j=1}^{J}(a_{04}^{(i,j)}\gamma_4^{[j]} + a_{05}^{(i,j)}\gamma_5^{[j]}), \quad \alpha_1^{(i)} = \sum_{j=1}^{J}(a_{14}^{(i,j)}\gamma_4^{[j]} + a_{15}^{(i,j)}\gamma_5^{[j]}), \quad \alpha_2^{(i)} = \sum_{j=1}^{J}(a_{24}^{(i,j)}\gamma_4^{[j]} + a_{25}^{(i,j)}\gamma_5^{[j]}),\\
\beta_0^{(i)} = \sum_{j=1}^{J}(b_{04}^{(i,j)}\gamma_4^{[j]} + b_{05}^{(i,j)}\gamma_5^{[j]}), \quad \beta_1^{(i)} = \sum_{j=1}^{J}(b_{14}^{(i,j)}\gamma_4^{[j]} + b_{15}^{(i,j)}\gamma_5^{[j]}), \quad \beta_2^{(i)} = \sum_{j=1}^{J}(b_{24}^{(i,j)}\gamma_4^{[j]} + b_{25}^{(i,j)}\gamma_5^{[j]}),
\end{gathered} \tag{7}$$

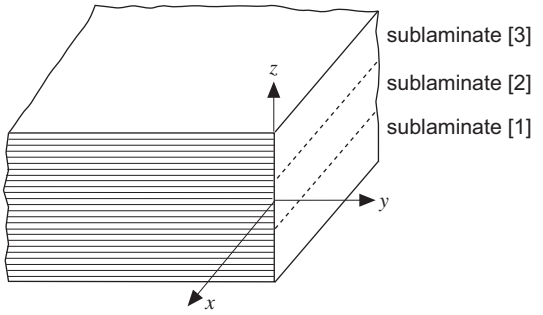

Fig. 3. A functionally graded plate divided into I layers and 3 sublaminates.

where $i = 1, \ldots, I$. Moreover, $a_{kl}^{(i,j)}$ and $b_{kl}^{(i,j)}$ are entries of $[A]$ and are constants determined by material properties and thickness coordinates of layers. Hence it follows from Eq. (1) that the displacement field of the ith layer can be presented in the following form:

$$\begin{aligned} u_1^{(i)} &= u - w_x z + \gamma_5^{(i)} z + \sum_{j=1}^{J} (\gamma_4^{[j]} g_{14}^{(i,j)} + \gamma_5^{[j]} g_{15}^{(i,j)}), \\ u_2^{(i)} &= v - w_y z + \gamma_4^{(i)} z + \sum_{j=1}^{J} (\gamma_4^{[j]} g_{24}^{(i,j)} + \gamma_5^{[j]} g_{25}^{(i,j)}), \\ u_3^{(i)} &= w, \end{aligned} \tag{8}$$

where

$$\begin{aligned} g_{14}^{(i,j)} &= a_{04}^{(i,j)} + a_{14}^{(i,j)} z^2 + a_{24}^{(i,j)} z^3, \quad g_{15}^{(i,j)} = a_{05}^{(i,j)} + a_{15}^{(i,j)} z^2 + a_{25}^{(i,j)} z^3, \\ g_{24}^{(i,j)} &= b_{04}^{(i,j)} + b_{14}^{(i,j)} z^2 + b_{24}^{(i,j)} z^3, \quad g_{25}^{(i,j)} = b_{05}^{(i,j)} + b_{15}^{(i,j)} z^2 + b_{25}^{(i,j)} z^3, \end{aligned} \tag{9}$$

$g_{15}^{(i,j)}$ and $g_{24}^{(i,j)}$ are shear warping functions, and $g_{14}^{(i,j)}$ and $g_{25}^{(i,j)}$ represent shear coupling functions. It follows from Eqs. (8) and (2) that the strains are given by

$$\begin{aligned} \varepsilon_{13}^{(i)} &= \gamma_5^{(i)} + \sum_{j=1}^{J} (\gamma_4^{[j]} g_{14z}^{(i,j)} + \gamma_5^{[j]} g_{15z}^{(i,j)}), \\ \varepsilon_{23}^{(i)} &= \gamma_4^{(i)} + \sum_{j=1}^{J} (\gamma_4^{[j]} g_{24z}^{(i,j)} + \gamma_5^{[j]} g_{25z}^{(i,j)}), \\ \varepsilon_{12}^{(i)} &= u_y + v_x - 2z w_{xy} + z\gamma_{5y}^{(i)} + z\gamma_{4x}^{(i)} \\ &\quad + \sum_{j=1}^{J} (\gamma_{4x}^{[j]} g_{24}^{(i,j)} + \gamma_{5x}^{[j]} g_{25}^{(i,j)} + \gamma_{4y}^{[j]} g_{14}^{(i,j)} + \gamma_{5y}^{[j]} g_{15}^{(i,j)}), \\ \varepsilon_{11}^{(i)} &= u_x - z w_{xx} + z\gamma_{5x}^{(i)} + \sum_{j=1}^{J} (\gamma_{4x}^{[j]} g_{14}^{(i,j)} + \gamma_{5x}^{[j]} g_{15}^{(i,j)}), \\ \varepsilon_{22}^{(i)} &= v_y - z w_{yy} + z\gamma_{4y}^{(i)} + \sum_{j=1}^{J} (\gamma_{4y}^{[j]} g_{24}^{(i,j)} + \gamma_{5y}^{[j]} g_{25}^{(i,j)}), \\ \varepsilon_{33}^{(i)} &= 0. \end{aligned} \tag{10}$$

The analysis will be based on a linear, uncoupled thermoelasticity theory, where the heat generated by elastic straining is assumed to be a negligible second-order effect and the influences of structural deformation on the thermal domain and thermal properties are also neglected. Hence, for an FGP subjected to

thermomechanical loads, strains due to thermal expansion can be linearly added to the mechanical strains, and the mechanical stress–strain relation of the ith layer can be written as [16–18]

$$\begin{aligned}\{\sigma^{(i)}\} &= [Q^{(i)}](\{\varepsilon^{(i)}\} - \{\Lambda^{(i)}\}\tau) \\ &= [Q^{(i)}]\left([S_2]\{\psi_2\} + \sum_{j=1}^{J}[S_3^{(i,j)}]\{\psi_3^{[j]}\} - \{\Lambda^{(i)}\}\tau\right) = [Q^{(i)}]([S^{(i)}]\{\psi\} - \{\Lambda^{(i)}\}\tau),\end{aligned} \tag{11}$$

where

$$\{\sigma^{(i)}\} \equiv \{\sigma_{11}^{(i)}, \sigma_{22}^{(i)}, \sigma_{23}^{(i)}, \sigma_{13}^{(i)}, \ \sigma_{12}^{(i)}\}^{\mathrm{T}},$$

$$\{\varepsilon^{(i)}\} \equiv \{\varepsilon_{11}^{(i)}, \ \varepsilon_{22}^{(i)}, \varepsilon_{23}^{(i)}, \ \varepsilon_{13}^{(i)}, \ \varepsilon_{12}^{(i)}\}^{\mathrm{T}},$$

$$\{\Lambda^{(i)}\} \equiv \{\Lambda_1^{(i)}, \ \Lambda_2^{(i)}, \ 0, \ 0, \ \Lambda_{12}^{(i)}\}^{\mathrm{T}},$$

$$\Lambda_1^{(i)} = \hat{\alpha}_1\cos^2\theta + \hat{\alpha}_2\sin^2\theta, \quad \Lambda_2^{(i)} = \hat{\alpha}_1\sin^2\theta + \hat{\alpha}_2\cos^2\theta, \quad \Lambda_{12}^{(i)} = 2(\hat{\alpha}_1 - \hat{\alpha}_2)\cos\theta\sin\theta,$$

$$\{\psi_2\} \equiv \{u_x, v_y, u_y + v_x, w_{xx}, w_{yy}, w_{xy}\}^{\mathrm{T}},$$

$$\{\psi_3^{[j]}\} \equiv \{\gamma_{4x}^{[j]}, \gamma_{4y}^{[j]}, \gamma_{5x}^{[j]}, \gamma_{5y}^{[j]}, \gamma_4^{[j]}, \gamma_5^{[j]}\}^{\mathrm{T}},$$

$$\{\psi\} \equiv \{\{\psi_2\}^{\mathrm{T}}, \{\psi_3^{[1]}\}^{\mathrm{T}}, \ldots, \{\psi_3^{[J]}\}^{\mathrm{T}}\}^{\mathrm{T}},$$

$$[S_2] \equiv \begin{bmatrix} 1 & 0 & 0 & -z & 0 & 0 \\ 0 & 1 & 0 & 0 & -z & 0 \\ 0 & 0 & 0 & 0 & 0 & 0 \\ 0 & 0 & 0 & 0 & 0 & 0 \\ 0 & 0 & 1 & 0 & 0 & -2z \end{bmatrix},$$

$$[S_3^{(i,j)}] \equiv \begin{bmatrix} g_{14} & 0 & z\delta_{ij} + g_{15} & 0 & 0 & 0 \\ 0 & z\delta_{ij} + g_{24} & 0 & g_{25} & 0 & 0 \\ 0 & 0 & 0 & 0 & \delta_{ij} + g_{24z} & g_{25z} \\ 0 & 0 & 0 & 0 & g_{14z} & \delta_{ij} + g_{15z} \\ z\delta_{ij} + g_{24} & g_{14} & g_{25} & z\delta_{ij} + g_{15} & 0 & 0 \end{bmatrix}^{(i,j)}. \tag{12}$$

Here τ is the temperature increase beyond the reference temperature of the stress-free reference configuration, $\hat{\alpha}_1$ and $\hat{\alpha}_2$ are thermal expansion coefficients with respect to the material axes $\hat{x}$ and $\hat{y}$, respectively, θ is the rotation angle from the $\hat{x}$-axis to the x-axis, and $[Q^{(i)}]$ is the transformed and reduced (because $\sigma_{33} = 0$) material stiffness matrix. Moreover, $\delta_{ij} = 1$ if the ith layer is within the jth sublaminate (i.e., $\gamma_4^{(i)} = \gamma_4^{[j]}$), and $\delta_{ij} = 0$ if the ith layer is not within the jth sublaminate. Note that the δ_{ij} used here is not the regular Dirac delta function. For example, if the second layer is within the first sublaminate, $\delta_{21} = 1$ and $\delta_{22} = 0$. We note that, even if an FGP is fabricated by a continuous grading method, this method also works because the plate can be artificially divided into I layers with material properties being those at the mid-point of each layer. The transverse shears due to non-uniform thermal expansion through the plate thickness are assumed to be negligible, and the temperature distribution can be assumed in the following form:

$$\tau(x, y, z, t) = \tau_1(x, y, t)\tau_2(z). \tag{13}$$

2.2. Effective mechanical and thermal properties

Mechanical properties of an FGP include Young's modulus E, shear modulus G, Poisson's ratio v, and mass density ρ, and thermal properties include the coefficient of thermal expansion $\hat{\alpha}$, the thermal conductivity k, and the specific heat capacity c. ρ and v are usually linear functions of material volume ratios, but others are nonlinear functions of material volume ratios because they depend on material microstructures [9]. The FGP theory presented here can work with effective material properties estimated by using any method. For the purpose of demonstration, the effective properties P (e.g., E and α) will be estimated using the simple, Voigt method (i.e., an arithmetic method) as

$$P = P_1 V_1 + P_2 V_2, \quad V_1 + V_2 = 1, \tag{14}$$

where P_1 and P_2 are the properties of the first and second constituent materials (e.g., metal and ceramic), and V_1 and V_2 are the volume fractions of the constituent materials. The distributions of volume fractions through the plate thickness are assumed to follow the following simple power law:

$$V_2 = \left(\frac{z - \overline{z}_1}{z_{I+1} - z_1}\right)^n, \tag{15}$$

where n can be any non-negative real number, and $\overline{z}_1 \leqslant z_1$. Note that $V_2 = 0$ at $z = z_1$ if $\overline{z}_1 = z_1$, and $V_2 > 0$ at $z = z_1$ if $\overline{z}_1 < z_1$. Hence, we have

$$P = P_1 + (P_2 - P_1)\left(\frac{z - \overline{z}_1}{z_{I+1} - z_1}\right)^n. \tag{16}$$

Most of mechanical and thermal properties are linear or nonlinear functions of temperature, but ρ and v are usually independent of temperature. If a property P is a linear function of temperature, one can assume that

$$P = P_0(1 + \hat{P}\tau), \tag{17}$$

where τ is the temperature beyond the reference temperature and P and $\hat{P}$ are constant. For detailed modeling of effective material properties of FGMs the reader is referred to Refs. [3,9].

3. Finite-element formulation

The extended Hamilton principle states [19]

$$\int_0^t (\delta K_e - \delta \Pi + \delta W_{\text{nc}})\,\mathrm{d}t = 0, \tag{18}$$

where K_e is the kinetic energy, Π the elastic energy, and W_{nc} the non-conservative energy due to external distributed and/or concentrated loads and dampings.

3.1. Elastic energy

It follows from Eqs. (11)–(13) that

$$\delta \Pi = \sum_{i=1}^{I} \int_A \int_{z_i}^{z_{i+1}} \{\delta \varepsilon^{(i)}\}^{\mathrm{T}} \{\sigma^{(i)}\}\,\mathrm{d}z\,\mathrm{d}A = \int_A \{\delta\psi\}^{\mathrm{T}} ([\Phi]\{\psi\} - \{\hat{\Phi}\}\tau_1)\,\mathrm{d}A, \tag{19}$$

where A denotes the area of the reference plane, and z_i and z_{i+1} indicate the locations of the lower and upper surfaces of the ith layer. Moreover, $[\Phi]$ is a $(6 + 6J) \times (6 + 6J)$ symmetric matrix and $\{\hat{\Phi}\}$ is a $(6 + 6J) \times 1$ vector, which are defined as

$$[\Phi] = \sum_{i=1}^{I} \int_{z_i}^{z_{i+1}} [S^{(i)}]^{\mathrm{T}} [Q^{(i)}][S^{(i)}]\,\mathrm{d}z, \quad \{\hat{\Phi}\} = \sum_{i=1}^{I} \int_{z_i}^{z_{i+1}} [S^{(i)}]^{\mathrm{T}} [Q^{(i)}]\{\Lambda^{(i)}\}\tau_2(z)\,\mathrm{d}z. \tag{20}$$

Because the heat generated by elastic straining is negligible, the influences of elastic deformations on plate's geometry and thermal properties are neglected, and the variation frequency of temperature is assumed to be much lower than the mechanical vibration frequency, the temperature τ can be solved separately using the heat transfer equation. Consequently, τ can be treated as a known dependent variable for the mechanical problem here and hence $\delta\tau = 0$ is used. The integration of Eq. (20) can be obtained using Gauss quadratures [20].

Using the finite-element discretization scheme, we discretize the displacements as

$$\{u, v, w, \gamma_4^{[1]}, \gamma_5^{[1]}, \ldots, \gamma_4^{[J]}, \gamma_5^{[J]}\}^{\mathrm{T}} = [N]\{q^{[n]}\}, \tag{21}$$

where $\{q^{[n]}\}$ is the displacement vector of the nth element and $[N]$ is a matrix of 2D shape functions. Here four-node quadrilateral elements are assumed to be used. Each node has $6+2J$ degrees of freedom (dof) (i.e., $u, v, w, w_y, -w_x, w_{xy}, \gamma_4^{[1]}, \gamma_5^{[1]}, \ldots, \gamma_4^{[J]}, \gamma_5^{[J]}$). Hence $[N]$ is a $(3+2J)\times(24+8J)$ matrix. Moreover,

$$\{\psi\} = [D]\{q^{[n]}\}, \quad [D] \equiv [\hat{\partial}][N], \tag{22}$$

where $[\hat{\partial}]$ is a $(6+6J)\times(3+2J)$ matrix consisting of differential operators, and $[D]$ is a $(6+6J)\times(24+8J)$ matrix.

Substituting Eq. (22) into Eq. (19) yields

$$\begin{aligned}\delta\Pi &= \sum_{n=1}^{N_e}\int_{A^{[n]}}\{\delta q^{[n]}\}^{\mathrm{T}}[D]^{\mathrm{T}}([\Phi][D]\{q^{[n]}\} - \{\hat{\Phi}\}\tau_1)\,\mathrm{d}A = \sum_{n=1}^{N_e}\{\delta q^{[n]}\}^{\mathrm{T}}([K^{[n]}]\{q^{[n]}\} - \{\hat{F}^{[n]}\})\\ &= \{\delta q\}^{\mathrm{T}}([K]\{q\} - \{\hat{F}\}),\end{aligned} \tag{23}$$

where

$$[K^{[n]}] \equiv \int_{A^{[n]}}[D]^{\mathrm{T}}[\Phi][D]\,\mathrm{d}A, \quad \{\hat{F}^{[n]}\} \equiv \int_{A^{[n]}}[D]^{\mathrm{T}}\{\hat{\Phi}\}\tau_1\,\mathrm{d}A, \tag{24}$$

N_e is the total number of elements, $A^{[n]}$ is the area of the nth element, $[K^{[n]}]$ is the stiffness matrix of the nth element, $[K]$ is the structural stiffness matrix, $\{\hat{F}^{[n]}\}$ is the thermal-induced mechanical loading, and $\{q\}$ is the structural displacement vector.

3.2. Kinetic energy

The displacement field shown in Eq. (8) can be rewritten as

$$\{u^{(i)}\} = [\overline{S}_2]\{\overline{\psi}_2\} + \sum_{j=1}^{J}[\overline{S}_3^{(i,j)}]\{\overline{\psi}_3^{(j)}\} = [\overline{S}^{(i)}]\{\overline{\psi}\}, \tag{25}$$

where

$$\{u^{(i)}\} \equiv \{u_1^{(i)}, u_2^{(i)}, u_3^{(i)}\}^{\mathrm{T}},$$

$$\{\overline{\psi}_2\} \equiv \{u, v, w, w_x, w_y\}^{\mathrm{T}}, \quad \{\overline{\psi}_3^{[j]}\} \equiv \{\gamma_4^{[j]}, \gamma_5^{[j]}\}^{\mathrm{T}}, \quad \{\overline{\psi}\} \equiv \{\{\overline{\psi}_2\}^{\mathrm{T}}, \{\overline{\psi}_3^{[1]}\}^{\mathrm{T}}, \ldots, \{\overline{\psi}_3^{[J]}\}^{\mathrm{T}}\}^{\mathrm{T}},$$

$$[\overline{S}_2] \equiv \begin{bmatrix}1 & 0 & 0 & -z & 0\\ 0 & 1 & 0 & 0 & -z\\ 0 & 0 & 1 & 0 & 0\end{bmatrix}, \quad [\overline{S}_3^{(i,j)}] \equiv \begin{bmatrix} g_{14} & z\delta_{ij} + g_{15}\\ z\delta_{ij} + g_{24} & g_{25}\\ 0 & 0\end{bmatrix}^{(i,j)}. \tag{26}$$

Hence, the variation of kinetic energy is given by

$$\begin{aligned}\delta K_e &= -\sum_{i=1}^{I}\int_A\int_{z_i}^{z_{i+1}}\{\delta u^{(i)}\}^{\mathrm{T}}\rho^{(i)}\{\ddot{u}^{(i)}\}\,\mathrm{d}z\,\mathrm{d}A\\ &= -\int_A\{\delta\overline{\psi}\}^{\mathrm{T}}[\overline{\Phi}]\{\ddot{\overline{\psi}}\}\,\mathrm{d}A,\end{aligned} \tag{27}$$

where $\rho^{(i)}$ is the mass density of the ith layer, and $[\overline{\Phi}]$ is a $(5+2J)\times(5+2J)$ symmetric matrix given by

$$[\overline{\Phi}]=\sum_{i=1}^{I}\int_{z_i}^{z_{i+1}}[\overline{S}^{(i)}]^{\mathrm{T}}\rho^{(i)}[\overline{S}^{(i)}]\,\mathrm{d}z. \tag{28}$$

Using the same discretization scheme used in Eqs. (21) and (22), we obtain that

$$\{\overline{\psi}\}=[\overline{D}]\{q^{[n]}\},\quad [\overline{D}]\equiv[\overline{\partial}][N], \tag{29}$$

where $[\overline{\partial}]$ is a $(5+2J)\times(3+2J)$ matrix consisting of differential operators, and $[\overline{D}]$ is a $(5+2J)\times(24+8J)$ matrix.

Substituting Eq. (29) into Eq. (27) yields

$$\begin{aligned}\delta K_e &= -\sum_{n=1}^{N_e}\int_{A^{[n]}}\{\delta q^{[n]}\}^{\mathrm{T}}[\overline{D}]^{\mathrm{T}}[\overline{\Phi}][\overline{D}]\{\ddot{q}^{[n]}\}\,\mathrm{d}A=-\sum_{n=1}^{N_e}\{\delta q^{[n]}\}^{\mathrm{T}}[M^{[n]}]\{\ddot{q}^{[n]}\}\\ &= -\{\delta q\}^{\mathrm{T}}[M]\{\ddot{q}\},\end{aligned} \tag{30}$$

where

$$[M^{[n]}]\equiv\int_{A^{[n]}}[\overline{D}]^{\mathrm{T}}[\overline{\Phi}][\overline{D}]\,\mathrm{d}A, \tag{31}$$

$[M^{[n]}]$ is the mass matrix of the nth element and $[M]$ is the structural mass matrix.

3.3. External loads

For the non-conservative virtual work we only consider the external transverse distributed load f_3 and obtain that

$$\delta W_{\mathrm{nc}}=\int_A f_3\delta w\,\mathrm{d}A=\sum_{n=1}^{N_e}\int_{A^{[n]}}\{\delta q^{[n]}\}^{\mathrm{T}}\{N_3\}f_3\,\mathrm{d}A=\sum_{n=1}^{N_e}\{\delta q^{[n]}\}^{\mathrm{T}}\{F^{[n]}\}=\{\delta q\}^{\mathrm{T}}\{F\}, \tag{32}$$

where $\{N_3\}$ is the transpose of the third row of the $[N]$ shown in Eq. (21) and

$$\{F^{[n]}\}\equiv\int_{A^{[n]}}\{N_3\}f_3\,\mathrm{d}A. \tag{33}$$

3.4. Equation of motion

Substituting Eqs. (23), (30), and (32) into Eq. (18) yields the equation of motion as

$$[M]\{\ddot{q}\}+[C]\{\dot{q}\}+[K]\{q\}=\{F\}+\{\hat{F}\}, \tag{34}$$

where a damping matrix $[C]$ is added. Note that this SPE is a 2D one but it accounts for 3D effects caused by transverse shear stresses. This linear plate element is a new addition to the finite-element code geometrically exact structural analysis (GESA), which is written using MATLAB syntax and is mainly for analysis of highly flexible structures.

4. Numerical results

4.1. Shear warping functions

To show shear warping functions we consider an orthotropic laminate studied by Pagano [10,11]. The properties of each graphite/epoxy layer are

$$E_{11}=172.38\,\mathrm{GPa},\quad E_{22}=6.90\,\mathrm{GPa},\quad E_{33}=6.90\,\mathrm{GPa},\quad \nu_{12}=0.25,\quad \nu_{13}=0.25,\quad \nu_{23}=0.25,$$

$$G_{12} = 3.45\,\text{GPa}, \quad G_{13} = 3.45\,\text{GPa}, \quad G_{23} = 1.38\,\text{GPa}, \quad \hat{h} = 0.127\,\text{mm}, \tag{35}$$

where $\hat{h}$ is the layer thickness. If three sublaminates are assumed (i.e., $J = 3$), it follows from Eq. (8) that shear warpings $W_1^{(i)}$ and $W_2^{(i)}$ are given by

$$\begin{aligned} W_1^{(i)} &\equiv u_1^{(i)} - u + w_x z = \sum_{j=1}^{J} (\gamma_4^{[j]} g_{14}^{(i,j)} + \gamma_5^{[j]} (\delta_{ij} z + g_{15}^{(i,j)})) \\ &= \gamma_5^{(i)} z + \gamma_4^{[1]} g_{14}^{(i,1)} + \gamma_5^{[1]} g_{15}^{(i,1)} + \gamma_4^{[2]} g_{14}^{(i,2)} + \gamma_5^{[2]} g_{15}^{(i,2)} + \gamma_4^{[3]} g_{14}^{(i,3)} + \gamma_5^{[3]} g_{15}^{(i,3)}, \\ W_2^{(i)} &\equiv u_2^{(i)} - v + w_y z = \sum_{j=1}^{J} (\gamma_4^{[j]} (\delta_{ij} z + g_{24}^{(i,j)}) + \gamma_5^{[j]} g_{25}^{(i,j)}) \\ &= \gamma_4^{(i)} z + \gamma_4^{[1]} g_{24}^{(i,1)} + \gamma_5^{[1]} g_{25}^{(i,1)} + \gamma_4^{[2]} g_{24}^{(i,2)} + \gamma_5^{[2]} g_{25}^{(i,2)} + \gamma_4^{[3]} g_{24}^{(i,3)} + \gamma_5^{[3]} g_{25}^{(i,3)}, \end{aligned} \tag{36}$$

where $W_1^{(i)}$ is the shear warping of the yz cross section and $W_2^{(i)}$ is the shear warping of the xz cross section. Note that the δ_{ij} is not the regular Dirac delta function. $\delta_{ij} = 1$ if the ith layer is within the jth sublaminate even if $i \neq j$, and $\delta_{ij} = 0$ if the ith layer is not within the jth sublaminate even if $i = j$. Also, it follows from Eqs. (3) and (10) that

$$\begin{Bmatrix} \sigma_{23}^{(i)} \\ \sigma_{13}^{(i)} \end{Bmatrix} = \begin{bmatrix} Q_{44}^{(i)} & Q_{45}^{(i)} \\ Q_{45}^{(i)} & Q_{55}^{(i)} \end{bmatrix} \begin{Bmatrix} \sum_{j=1}^{J} (\gamma_4^{[j]} (\delta_{ij} + g_{24z}^{(i,j)}) + \gamma_5^{[j]} g_{25z}^{(i,j)}) \\ \sum_{j=1}^{J} (\gamma_4^{[j]} g_{14z}^{(i,j)} + \gamma_5^{[j]} (\delta_{ij} + g_{15z}^{(i,j)})) \end{Bmatrix}. \tag{37}$$

For a $[0^\circ/90^\circ/0^\circ]$ laminate, numerical results confirm that $Q_{45}^{(i)} = 0$ and shear coupling functions $g_{14}^{(i,j)}$ and $g_{25}^{(i,j)}$ are always zero for orthotropic cross-ply laminates [21]. Fig. 4 shows the shear warping functions $g_{kl}^{(ij)}$ and their contributions to the transverse shear stresses (see Eq. (37)). For this case, the ith layer is defined to be the ith sublaminate. The bottom and top layers are the first and third layers, respectively. Note that each of the shear warping functions of every sublaminate is continuous and its contribution to σ_{k3} is also continuous although $\delta_{ij} + g_{24z}^{(i,j)}$ and $\delta_{ij} + g_{15z}^{(i,j)}$ are discontinuous. Because three sublaminates are used, $\gamma_4^{[i]}$ and $\gamma_5^{[i]}$ $(i = 1, 2, 3)$ are six independent variables, and their relations depend on boundary and loading conditions. If $(\gamma_4^{[1]}, \gamma_4^{[2]}, \gamma_4^{[3]}) = (1, 1, 1)\gamma_4$ and $(\gamma_5^{[1]}, \gamma_5^{[2]}, \gamma_5^{[3]}) = (1, 1, 1)\gamma_5$ are assumed, Fig. 5 shows the shear warpings W_i and transverse shear stresses σ_{i3}, where

$$\sigma_{13}^{(i)}/\gamma_5 = Q_{55}^{(i)} W_{1z}^{(i)}/\gamma_5, \quad \sigma_{23}^{(i)}/\gamma_4 = Q_{44}^{(i)} W_{2z}^{(i)}/\gamma_4. \tag{38}$$

The broken lines represent the exact distributions [10,11], which are functions of specified plate dimensions and boundary and loading conditions. We note that the predicted shear stresses do not match well with the exact ones because incomplete cubic polynomials are used to describe the cross-section warping, as shown in Eq. (1). Moreover, because the warping functions and shear stress distributions obtained by Pagano [10] are dependent on the boundary and loading conditions and the thickness-to-span ratio (see Figs. 4c and e of Ref. [10]), this discrepancy is also problem dependent.

If the answers obtained from a set of specified plate dimensions and boundary and loading conditions are $\gamma_4^{[j]} = (2, 1, 2)\gamma_4$ and $\gamma_5^{[j]} = (0.5, 1, 0.5)\gamma_5$, Fig. 6 shows the W_i and σ_{i3}. Note that they are close to those of Pagano [10,11].

If $\gamma_4^{[j]} = (-0.58, 1, -0.58)\gamma_4$ and $\gamma_5^{[j]} = (-0.375, 1, -0.375)\gamma_5$, Fig. 7 shows the W_i and σ_{i3}. At a clamped edge parallel to the y-axis, because $\sigma_{13} = 0$ at the bottom $(z = z_1)$ and top $(z = z_{I+1})$ surfaces and the reference plane should be parallel to the bottom and top surfaces, $w_x = 0$. Moreover, because $u_1^{(1)}(z_1) = u_1^{(I)}(z_{I+1}) = 0$ at the clamped edge,

$$\begin{aligned} W_1^{(1)}(z_1) &= 0 = \gamma_5^{[1]}(z_1 + g_{15}^{(1,1)}(z_1)) + \gamma_5^{[2]} g_{15}^{(1,2)}(z_1) + \gamma_5^{[3]} g_{15}^{(1,3)}(z_1), \\ W_1^{(I)}(z_{I+1}) &= 0 = \gamma_5^{[1]} g_{15}^{(I,1)}(z_{I+1}) + \gamma_5^{[2]} g_{15}^{(I,2)}(z_{I+1}) + \gamma_5^{[3]}(z_{I+1} + g_{15}^{(I,3)}(z_{I+1})). \end{aligned}$$

Hence, Fig. 7a can be used to simulate the restraint warping of a clamped plate edge parallel to the y-axis. This condition can be implemented in analysis by using two multiple point constraints. Similarly, $w_y = W_2 = 0$ on the bottom and top surfaces at a clamped edge parallel to the x-axis, and Fig. 7b can be used to simulate the

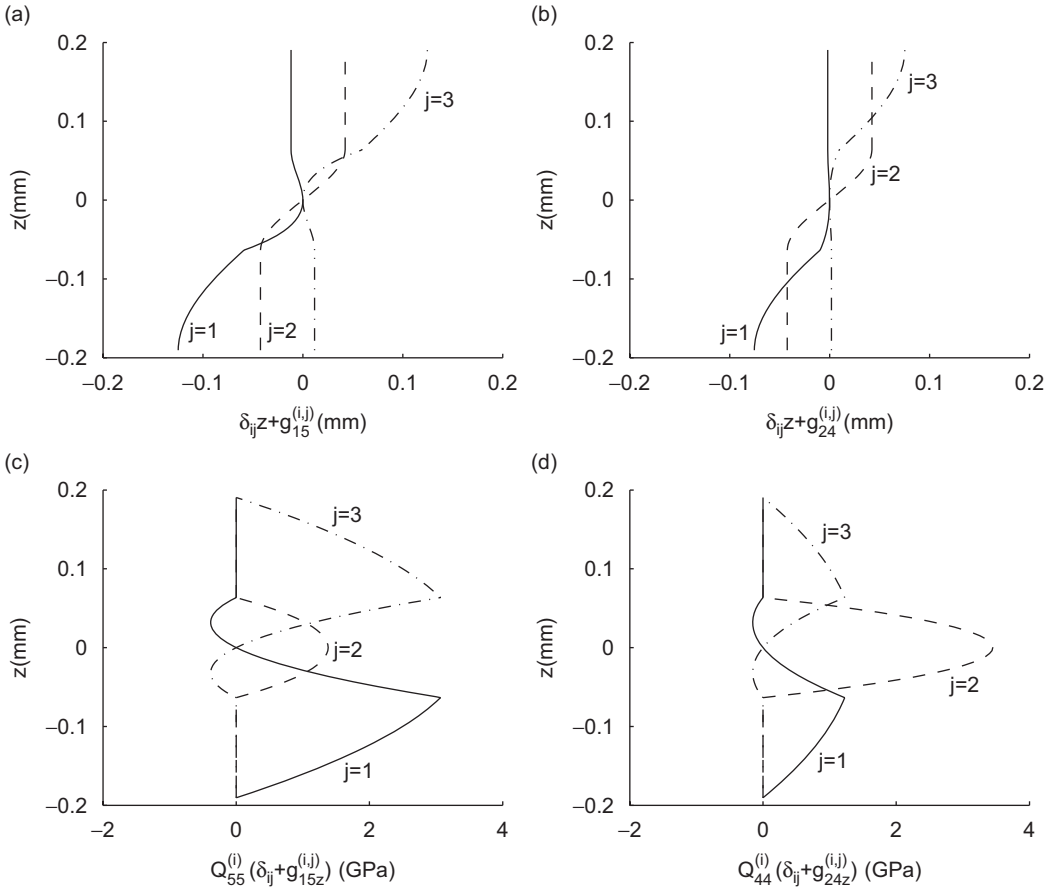

Fig. 4. Shear warping functions of a [0°/90°/0°] laminate: (a) $\delta_{ij}z+g_{15}^{(i,j)}$, (b) $\delta_{ij}z+g_{24}^{(i,j)}$, (c) $Q_{55}^{(i)}(\delta_{ij}+g_{15z}^{(i,j)})$, and (d) $Q_{44}^{(i)}(\delta_{ij}+g_{24z}^{(i,j)})$. The solid lines are of the first sublaminate ($j=1$), the dashed lines ($j=2$), and the dash-dot lines ($j=3$).

restraint warping of a clamped plate edge parallel to the x-axis. If the first-order shear-deformation theory is used, one needs to assign $w_y=\gamma_4\neq 0$ in order to have a non-zero shear force at a clamped plate edge parallel to the x-axis, which violates the actual boundary condition. It is apparent that the use of sublamination increases the freedom for accurate modeling of different boundary conditions.

It has been shown in the literature that shear warping functions may vary with the spatial location, vibration frequency, loading and boundary conditions, and structural dimensions [13,22]. The shear warping functions shown in Figs. 5–7a,b are very different, but each of them is continuous and has continuous σ_{k3}. The actual cross-sectional warpings depend on the ratios between $\gamma_5^{[j]}$ and $\gamma_4^{[j]}$, and $\gamma_5^{[j]}$ and $\gamma_4^{[j]}$ are determined by loading and boundary conditions. Apparently, the use of sublamination and more dependent variables enables the modeling of such deformation-dependent shear warping functions. If each layer is treated as a sublaminate, the number of dependent variables will be $3+2I$ (i.e., u, v, w, $\gamma_4^{(1)}$, $\gamma_5^{(1)}$,…, $\gamma_4^{(I)}$, $\gamma_5^{(I)}$) and the theory is equivalent to that in Ref. [23]. One can reduce the number of dependent variables by reducing the number of sublaminates by using specific ratios between $\gamma_4^{[j]}$ and $\gamma_5^{[j]}$, as shown in Figs. 5 and 6.

Next, we consider an orthotropic laminate studied by Noor and Burton [24]. The material properties of each layer are

$$E_{11}=103.43\,\text{GPa},\quad E_{22}=6.90\,\text{GPa},\quad E_{33}=6.90\,\text{GPa},\quad \nu_{12}=0.3,\quad \nu_{13}=0.3,\quad \nu_{23}=0.49,$$

$$G_{12}=3.45\,\text{GPa},\quad G_{13}=3.45\,\text{GPa},\quad G_{23}=2.42\,\text{GPa},\quad \hat{h}=0.127\,\text{mm}. \tag{39}$$

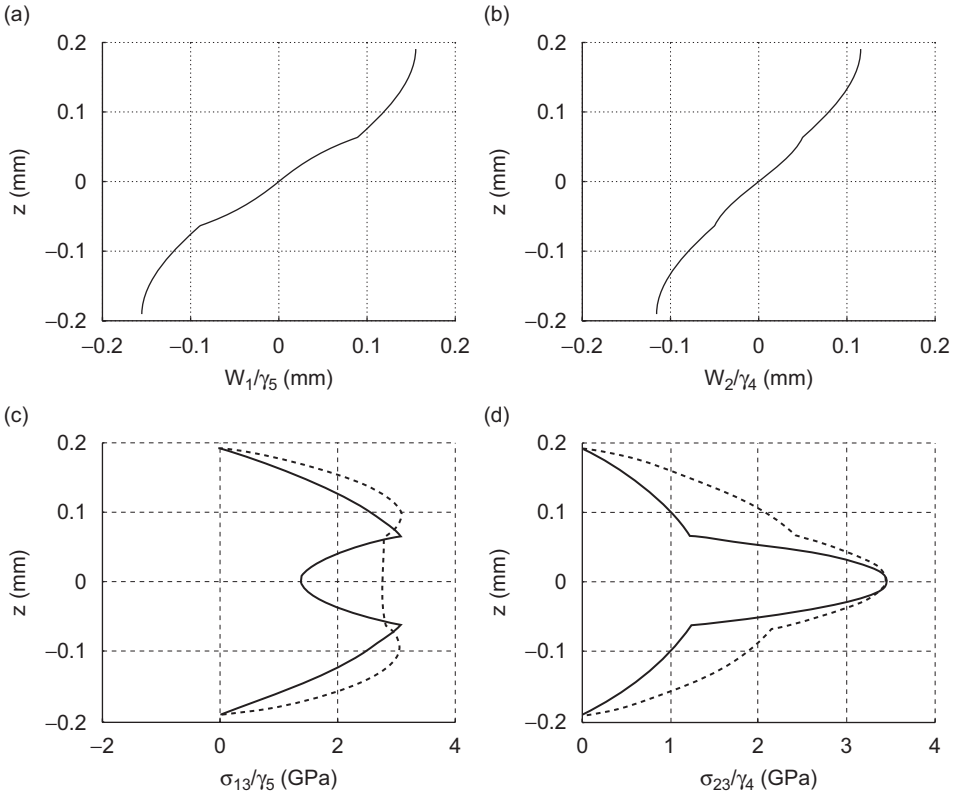

Fig. 5. A $[0^\circ/90^\circ/0^\circ]$ laminate: (a) shear warping W_1/γ_5, (b) shear warping W_2/γ_4, (c) shear stress σ_{13}/γ_5, and (d) shear stress σ_{23}/γ_4, where $\gamma_4^{[j]} = (1,1,1)\gamma_4$ and $\gamma_5^{[j]} = (1,1,1)\gamma_5$ are assumed and the broken lines are exact solutions.

For a $[0^\circ/90^\circ/0^\circ/90^\circ]$ laminate, Fig. 8 shows that the obtained distribution of σ_{13}/γ_5 (solid lines) is similar to the exact one (broken lines) obtained by Noor and Burton [24, Fig. 3], where the reference plane is chosen to be on the neutral axis of the yz cross section. Because the neutral axis of the xz cross section is different from that of the yz cross section, the obtained σ_{23}/γ_4 is not as accurate as σ_{13}/γ_5. For an anisotropic laminate, the neutral axis of the xz cross section may not be on the midplane, the neutral axis of the yz cross section may not be on the midplane, and these two neutral axes may not be on the same plane. These cause difficulties in and reveal complexity of the analysis of anisotropic laminates. However, for symmetric and skew-symmetric laminates, the neutral axes are always on the midplane. Because $\gamma_5^{[j]}$ $(j = 1,\ldots,4)$ are four independent variables, using different ratios between $\gamma_5^{[j]}$ may result in more accurate σ_{13}/γ_5, as shown in Fig. 8b. To improve the accuracy one can even divide the four layers into eight (or more) sublaminates, as shown in Fig. 8c. Similarly, this approach can be used to improve the accuracy of σ_{13} and σ_{23} in Figs. 6c and d by using more sublaminates.

For a 21-layer $[(0^\circ/90^\circ)_{10}/0^\circ]$ laminate, the shear warping functions and transverse shear stresses are shown in Fig. 9. We note that, although the shear warping functions and shear stresses are zigzag, their global distributions are very similar to those of an isotropic plate (i.e., a parabolic function $1 - 4z^2/h^2$). This is expected because the number of layers is high. It reveals that, for a laminate consisting of many layers, one can treat it just like an isotropic one, except that the reference plane is better to be on the neutral plane.

For general anisotropic laminates, shear coupling functions g_{14} and g_{25} are non-zero [21] and hence the distributions of σ_{13} and σ_{23} depend on the values of γ_4 and γ_5, which are determined by loading and boundary conditions and plate dimensions. However, FGPs are usually isotropic on the xy plane.

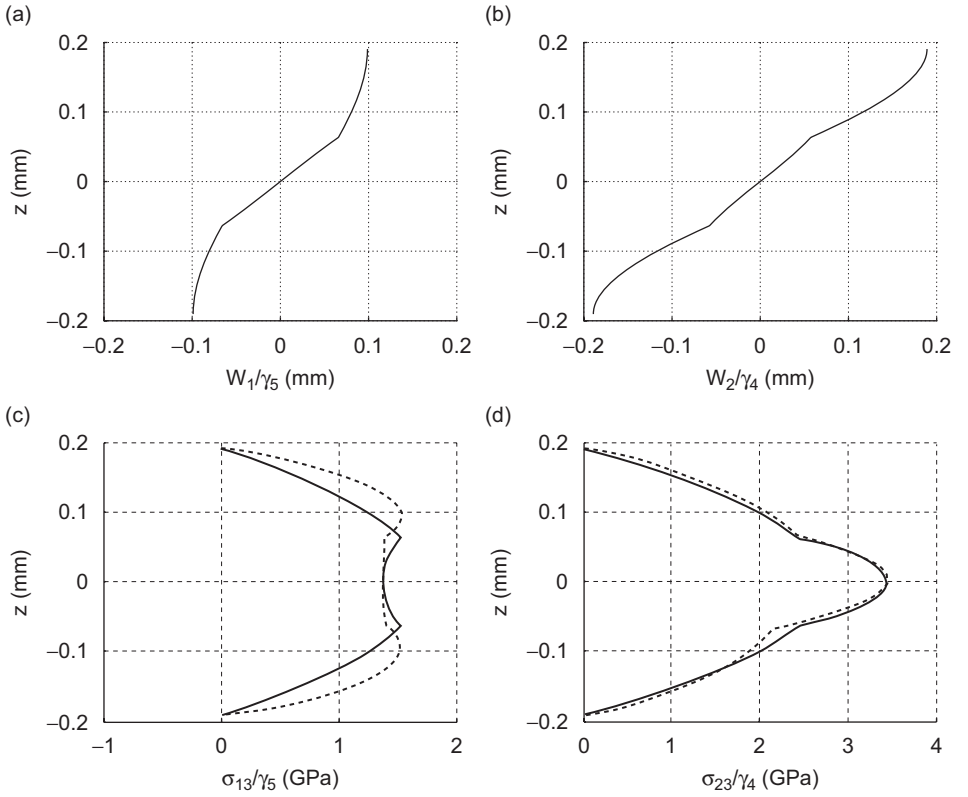

Fig. 6. A $[0^\circ/90^\circ/0^\circ]$ laminate: (a) W_1/γ_5, (b) W_2/γ_4, (c) σ_{13}/γ_5, and (d) σ_{23}/γ_4, where $\gamma_4^{[l]} = (2,1,2)\gamma_4$ and $\gamma_5^{[l]} = (0.5,1,0.5)\gamma_5$ and the broken lines are exact solutions.

4.2. Theory validation

To validate this 2D SPT in predicting all plate vibration modes we consider the free undamped vibration of a simply supported plate that was studied in Refs. [12,14].

For any mechanical system without body forces, the dynamic version of the principle of virtual work can be derived using the extended Hamilton principle to be [19]

$$\int_V \sum_{i=1}^{I}\sum_{k=1}^{3}(\sigma_{1kx}^{(i)} + \sigma_{2ky}^{(i)} + \sigma_{3kz}^{(i)} - \rho^{(i)}\ddot{u}_k^{(i)})\delta u_k^{(i)}\,\mathrm{d}V = 0, \tag{40}$$

where V is the system volume and $\sigma_{1kx} \equiv \partial\sigma_{1k}/\partial x$, etc. Hence, the equilibrium equations of a differential material particle are

$$\sigma_{1kx}^{(i)} + \sigma_{2ky}^{(i)} + \sigma_{3kz}^{(i)} = \rho^{(i)}\ddot{u}_k^{(i)}, \quad k = 1,2,3. \tag{41}$$

For a simply supported plate under free vibration the boundary conditions are given by [10]

$$u_2^{(i)} = u_3^{(i)} = \sigma_{11}^{(i)} = 0 \text{ at } x = 0,a, \quad i = 1,\ldots,I,$$

$$u_1^{(i)} = u_3^{(i)} = \sigma_{22}^{(i)} = 0 \text{ at } y = 0,b, \quad i = 1,\ldots,I,$$

$$\sigma_{13}^{(i)} = \sigma_{23}^{(i)}\ (= \sigma_{33}^{(i)}) = 0 \text{ at } z = \pm h/2, \quad i = 1,I. \tag{42}$$

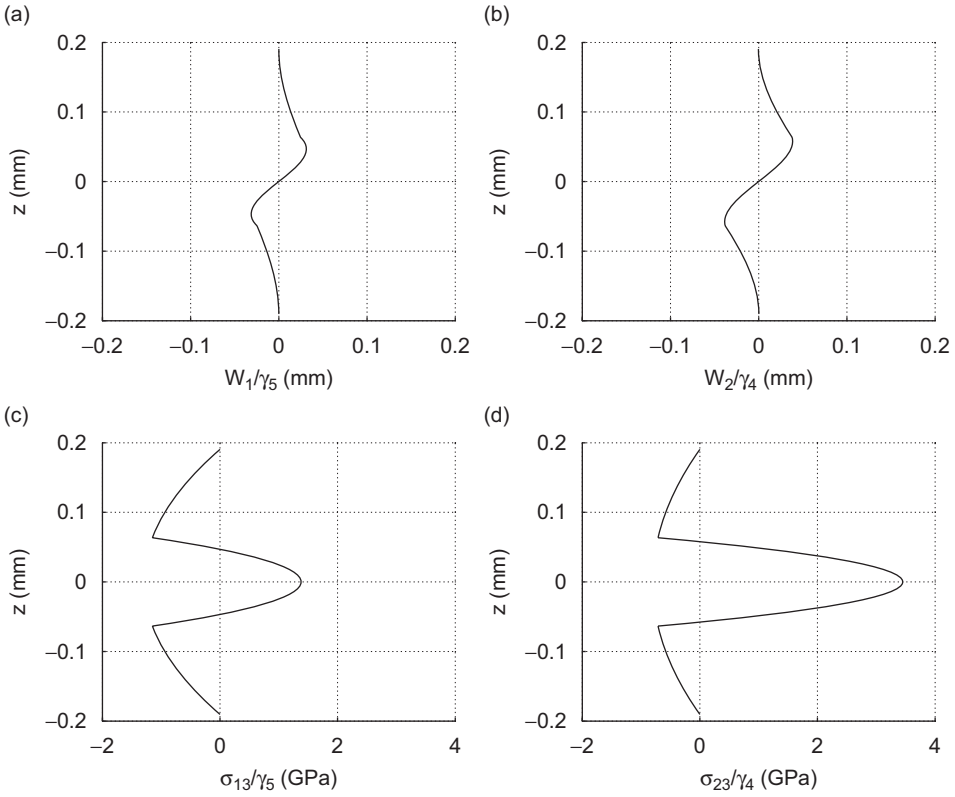

Fig. 7. A $[0^\circ/90^\circ/0^\circ]$ laminate: (a) W_1/γ_5, (b) W_2/γ_4, (c) σ_{13}/γ_5, and (d) σ_{23}/γ_4, where $\gamma_4^{[j]} = (-0.58, 1, -0.58)\gamma_4$ and $\gamma_5^{[j]} = (-0.375, 1, -0.375)\gamma_5$.

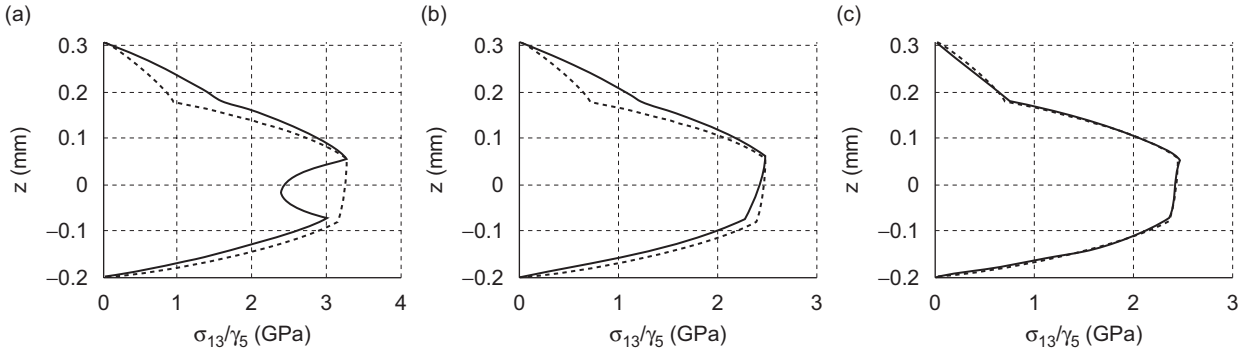

Fig. 8. The σ_{13}/γ_5 of a $[0^\circ/90^\circ/0^\circ/90^\circ]$ laminate: (a) $\gamma_5^{[j]} = (1, 1, 1, 1)\gamma_5$, (b) $\gamma_5^{[j]} = (0.76, 1, 0.76, 0.76)\gamma_5$, and (c) $\gamma_5^{[j]} = (0.9, 0.76, 1, 1, 0.77, 0.76, 0.5, 0.4)\gamma_5$. The broken lines are exact solutions.

An FGP is usually transversely isotropic. For an orthotropic laminate or a transversely isotropic plate its material stiffness matrix can be reduced by using $\sigma_{33} = 0$ (see Eq. (11)) to be

$$[Q^{(i)}] = \begin{bmatrix} Q_{11}^{(i)} & Q_{12}^{(i)} & 0 & 0 & 0 \\ Q_{21}^{(i)} & Q_{22}^{(i)} & 0 & 0 & 0 \\ 0 & 0 & Q_{44}^{(i)} & 0 & 0 \\ 0 & 0 & 0 & Q_{55}^{(i)} & 0 \\ 0 & 0 & 0 & 0 & Q_{66}^{(i)} \end{bmatrix}. \tag{43}$$

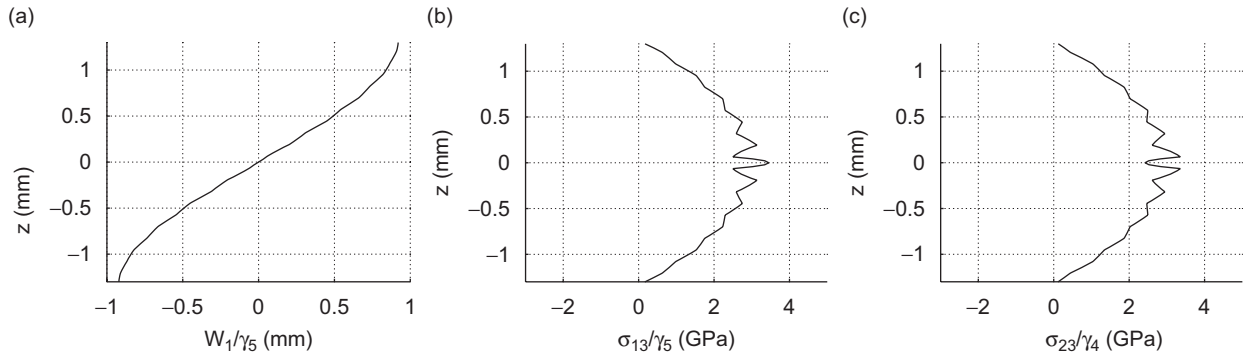

Fig. 9. A $[(0^\circ/90^\circ)_{10}/0^\circ]$ laminate: (a) W_1/γ_5, (b) σ_{13}/γ_5, and (c) σ_{23}/γ_4, where $\gamma_4^{[j]} = \gamma_4$ and $\gamma_5^{[j]} = \gamma_5$ are assumed.

The solutions of dependent variables that satisfy Eqs. (41) and (42) have the following forms:

$$u = U\cos\overline{m}x\sin\overline{n}y\sin\omega t, \quad v = V\sin\overline{m}x\cos\overline{n}y\sin\omega t, \quad w = W\sin\overline{m}x\sin\overline{n}y\sin\omega t,$$

$$\gamma_5^{(i)} = G_5^{(i)}\cos\overline{m}x\sin\overline{n}y\sin\omega t, \quad \gamma_4^{(i)} = G_4^{(i)}\sin\overline{m}x\cos\overline{n}y\sin\omega t, \quad \overline{m} \equiv m\pi/a, \quad \overline{n} \equiv n\pi/b \tag{44}$$

which can be proved by substituting Eq. (44) into Eqs. (8) and (10), then into Eq. (11) with $\tau = 0$ and $[Q^{(i)}]$ shown in Eq. (43), and then into Eq. (41), as shown next. Here the U, V, W, $G_4^{(i)}$, and $G_5^{(i)}$ are unknown constants, and ω is the unknown, undamped natural frequency. Because $g_{14}^{(i,j)} = g_{25}^{(i,j)} = 0$ for transversely isotropic plates, substituting Eq. (44) into Eq. (8) yields

$$u_1^{(i)} = U_1\cos\overline{m}x\sin\overline{n}y\sin\omega t, \quad u_2^{(i)} = V_1\sin\overline{m}x\cos\overline{n}y\sin\omega t, \quad u_3^{(i)} = W\sin\overline{m}x\sin\overline{n}y\sin\omega t,$$

$$U_1(z) \equiv U - W\overline{m}z + G_5^{(i)}z + \sum_{j=1}^{J} G_5^{[j]}g_{15}^{(i,j)}, \quad V_1(z) \equiv V - W\overline{n}z + G_4^{(i)}z + \sum_{j=1}^{J} G_4^{[j]}g_{24}^{(i,j)}. \tag{45}$$

Substituting Eq. (44) into Eq. (10) yields

$$\begin{aligned}
&\varepsilon_{13}^{(i)} = E_{13}^{(i)}\cos\overline{m}x\sin\overline{n}y\sin\omega t, \quad \varepsilon_{23}^{(i)} = E_{23}^{(i)}\sin\overline{m}x\cos\overline{n}y\sin\omega t,\\
&\varepsilon_{12}^{(i)} = E_{12}^{(i)}\cos\overline{m}x\cos\overline{n}y\sin\omega t, \quad \varepsilon_{11}^{(i)} = E_{11}^{(i)}\sin\overline{m}x\sin\overline{n}y\sin\omega t,\\
&\varepsilon_{22}^{(i)} = E_{22}^{(i)}\sin\overline{m}x\sin\overline{n}y\sin\omega t, \quad \varepsilon_{33}^{(i)} = E_{33}^{(i)}\sin\overline{m}x\sin\overline{n}y\sin\omega t,\\
&E_{13}^{(i)} \equiv G_5^{(i)} + \sum_{j=1}^{J} G_5^{[j]}g_{15z}^{(i,j)}, \quad E_{23}^{(i)} \equiv G_4^{(i)} + \sum_{j=1}^{J} G_4^{[j]}g_{24z}^{(i,j)},\\
&E_{12}^{(i)} \equiv U\overline{n} + V\overline{m} - 2zW\overline{m}\overline{n} + zG_5^{(i)}\overline{n} + zG_4^{(i)}\overline{m} + \sum_{j=1}^{J}(G_4^{[j]}\overline{m}g_{24}^{(i,j)} + G_5^{[j]}\overline{n}g_{15}^{(i,j)}),\\
&E_{11}^{(i)} \equiv -U\overline{m} + zW\overline{m}^2 - zG_5^{(i)}\overline{m} - \sum_{j=1}^{J} G_5^{[j]}\overline{m}g_{15}^{(i,j)},\\
&E_{22}^{(i)} \equiv -V\overline{n} + zW\overline{n}^2 - zG_4^{(i)}\overline{n} - \sum_{j=1}^{J} G_4^{[j]}\overline{n}g_{24}^{(i,j)}.
\end{aligned} \tag{46}$$

The $E_{ij}^{(i)}$ are known functions of z, U, V, W, $G_4^{(i)}$, and $G_5^{(i)}$. Substituting Eq. (46) into Eq. (11) with $\tau = 0$ and $[Q^{(i)}]$ given by Eq. (43) yields

$$\begin{aligned}
&\sigma_{11}^{(i)} = S_{11}^{(i)} \sin \overline{m}x \sin \overline{n}y \sin \omega t, \quad \sigma_{22}^{(i)} = S_{22}^{(i)} \sin \overline{m}x \sin \overline{n}y \sin \omega t,\\
&\sigma_{33}^{(i)} = S_{33}^{(i)} \sin \overline{m}x \sin \overline{n}y \sin \omega t, \quad \sigma_{23}^{(i)} = S_{23}^{(i)} \sin \overline{m}x \cos \overline{n}y \sin \omega t,\\
&\sigma_{13}^{(i)} = S_{13}^{(i)} \cos \overline{m}x \sin \overline{n}y \sin \omega t, \quad \sigma_{12}^{(i)} = S_{12}^{(i)} \cos \overline{m}x \cos \overline{n}y \sin \omega t,\\
&S_{11}^{(i)} \equiv Q_{11}^{(i)} E_{11}^{(i)} + Q_{12}^{(i)} E_{22}^{(i)}, \quad S_{22}^{(i)} \equiv Q_{21}^{(i)} E_{11}^{(i)} + Q_{22}^{(i)} E_{22}^{(i)}, \quad S_{33}^{(i)} = 0,\\
&S_{23}^{(i)} \equiv Q_{44}^{(i)} E_{23}^{(i)}, \quad S_{13} \equiv Q_{55}^{(i)} E_{13}^{(i)}, \quad S_{12} \equiv Q_{66}^{(i)} E_{12}^{(i)}.
\end{aligned} \tag{47}$$

The $S_{ij}^{(i)}$ are known functions of z, U, V, W, $G_4^{(i)}$, and $G_5^{(i)}$. Note that $S_{33}^{(i)} = 0$ for the proposed theory. If $u_3^{(i)} = w + \eta_1^{(i)} z + \eta_2^{(i)} z^2$ is assumed in Eq. (1), $E_{33}^{(i)}$ and $S_{33}^{(i)}$ will be also known functions of z, U, V, W, $G_4^{(i)}$, and $G_5^{(i)}$. However, $E_{33}^{(i)}$ and $S_{33}^{(i)}$ are neglected from the beginning because they are mainly caused by normal loads on the top and/or bottom surfaces and Poisson's effect, and they do not have significant influences on other stresses and strains [15].

Eq. (44) shows that the xy-plane distribution of $\gamma_4^{(i)}$ ($\gamma_5^{(i)}$) of every layer is the same and hence the ratios among $\gamma_4^{[j]}$ ($\gamma_5^{[j]}$) at any (x, y) location is the same. In other words, the shear warpings $W_1^{(i)}$ and $W_2^{(i)}$ are independent of x and y, and hence there is no boundary restraint effect in a simply supported plate. Substituting Eqs. (47) and (45) into Eq. (40) yields

$$\begin{aligned}
0 = &\sum_{i=1}^{I} \int_{z_i}^{z_{i+1}} [(\overline{m}S_{11}^{(i)} - \overline{n}S_{12}^{(i)} + S_{13z}^{(i)} + \rho\omega^2 U_1) C_s \delta U_1 + (-\overline{m}S_{12}^{(i)} + \overline{n}S_{22}^{(i)} + S_{23z}^{(i)} + \rho\omega^2 V_1) S_c \delta V_1\\
&+ (-\overline{m}S_{13}^{(i)} - \overline{n}S_{23}^{(i)} + \rho\omega^2 W) S_s \, \delta W] \, \mathrm{d}z \sin \omega t\\
= &\{\delta p\}^{\mathrm{T}} ([\tilde{A}] - \omega^2 [\tilde{B}]) \{p\} \sin \omega t,
\end{aligned}$$

$$\begin{aligned}
\{C_s, S_c, \ S_s\} &\equiv \int_0^a \int_0^b \{\cos^2 \overline{m}x \sin^2 \overline{n}y, \sin^2 \overline{m}x \cos^2 \overline{n}y, \sin^2 \overline{m}x \sin^2 \overline{n}y\} \, \mathrm{d}x \, \mathrm{d}y,\\
\{p\} &\equiv \{U, V, W, G_4^{[1]}, G_5^{[1]}, \ldots, G_4^{[J]}, G_5^{[J]}\}^{\mathrm{T}},
\end{aligned} \tag{48}$$

where $[\tilde{A}]$ and $[\tilde{B}]$ are $(3 + 2J) \times (3 + 2J)$ constant matrices. Note that the u, v, and w in Eq. (44) represent the in-plane (or reference plane) deformation mode shape and the $U_1(z)$ and $V_1(z)$ in Eq. (45) represent the thickness deformation mode shape. For a known in-plane mode shape, the thickness mode shapes and natural frequencies can be obtained by solving the following eigenvalue problem from Eq. (48)

$$([\tilde{A}] - \omega^2 [\tilde{B}]) \{p\} = \{0\}. \tag{49}$$

The transverse normal stress $S_{33}^{(i)}$ can be obtained by integrating the third equation of Eq. (41), i.e.

$$S_{33z}^{(i)} = \overline{m}S_{13}^{(i)} + \overline{n}S_{23}^{(i)} - \rho\omega^2 W \tag{50}$$

and setting $S_{33}^{(1)}(z_1) = 0$ at the bottom surface.

For a $5\,\mathrm{cm} \times 5\,\mathrm{cm} \times 1\,\mathrm{cm}$ aluminum plate with $E = 70\,\mathrm{GPa}$, $v = 0.3$, and $\rho = 2702\,\mathrm{kg/m^3}$, Table 1 compares the natural frequencies $\omega_{11,k}$ (i.e., $(m, n, k) = (1, 1, k)$) of vibration modes obtained from the SPT with the 3D elasticity solutions obtained by Vel and Batra [14] using a power series method. The natural frequencies $\omega_{11,k}$ are normalized to be non-dimensional as $\overline{\omega}_{11k} \equiv \omega_{11k} a^2 \sqrt{\rho/E}/h$. With the use of 3 layers and 3 sublaminates (i.e., $I = J = 3$), there are only 9 variables in the vector $\{p\}$ of Eqs. (48) and (49) and hence it can give only 9 natural frequencies. It is clear that all natural frequencies are close to the exact ones except $\overline{\omega}_{11,9}$. When the number of layers increases beyond 10, all the frequencies agree well with the exact ones. Fig. 10 shows the thickness-direction distributions of stresses S_{13}, S_{11}, and S_{33} of 6 modes obtained using 15 layers and 15 sublaminates (i.e., $I = J = 15$) and setting the maximum of the 15 $G_5^{[j]}$ to be one. All the S_{ij} are plotted using the same scale, but the S_{13} and S_{33} in Fig. 10a are small and hence they are magnified by 5 and 10 times, respectively. By scrutinizing the in-plane and thickness-direction distributions of U, V, W, U_1, V_1, W_i,

Table 1
The natural frequencies $\overline{\omega}_{11,k}$ of thickness modes of a 5 cm × 5 cm × 1 cm aluminum plate (the # indicates the mode number)

	Exact	SPT			SPE		Characteristics
	$a = 5h$	$J = I = 15$ layers	$J = I = 11$ layers	$J = I = 3$ layers	$J = I = 3$ layers	$J = I = 11$ layers	
$\overline{\omega}_{11,1}$	5.3036	5.2813	5.2813	5.2813	5.3606 (#1) (#1)	5.3605 (#1) (#1)	$U = V = 0$, $U_1 = V_1$, $W_1 = W_2$, $W \neq 0$, $S_{11} = S_{22}$, $S_{13} = S_{23}$ (BS)
$\overline{\omega}_{11,2}$	13.777	13.777	13.777	13.777	13.887 (#6) (#4)	13.887 (#6) (#4)	$U = -V = U_1 = -V_1$, $W = W_1 = W_2 = 0$, $S_{11} = -S_{22} = \text{const.}$, $S_{13} = S_{23} = S_{33} = 0$ (TC)
$\overline{\omega}_{11,3}$	23.136	23.287	23.287	23.287	23.351 (#14) (#9)	23.351 (#14) (#9)	$U = V = U_1 = V_1$, $W = W_1 = W_2 = 0$, $S_{11} = S_{22} = \text{const.}$, $S_{13} = S_{23} = 0$ (TT)
$\overline{\omega}_{11,4}$	50.619	50.619	50.619	50.634	50.642 (#52) (#29)	50.628 (#52) (#29)	$U = V = W = 0$, $U_1 = W_1 = -V_1 = -W_2$, $S_{11} = -S_{22}$, $S_{13} = -S_{23}$, $S_{33} = 0$ (S)
$\overline{\omega}_{11,5}$	54.727	55.146	55.146	55.162	55.170 (#67) (#42)	55.155 (#67) (#42)	$U = V = 0$, $U_1 = V_1$, $W_1 = W_2$, $W \neq 0$, $S_{11} = S_{22}$, $S_{13} = S_{23}$ (SB)
$\overline{\omega}_{11,7}$	98.386	98.395	98.411	99.442	99.458 (#214) (#151)	98.426 (#211) (#147)	$U = -V$, $W = 0$, $U_1 = -V_1$, $W_1 = -W_2$, $S_{11} = -S_{22}$, $S_{13} = -S_{23}$, $S_{33} = 0$ (STC)
$\overline{\omega}_{11,8}$	104.75	100.17	100.19	101.20	101.21 (#228) (#158)	100.20 (#225) (#158)	$U = V$, $W = 0$, $U_1 = V_1$, $W_1 = W_2$, $S_{11} = S_{22}$, $S_{13} = S_{23}$ (STT)
$\overline{\omega}_{11,9}$	146.01	148.04	148.08	163.63	163.64 (#532) (#412)	148.09 (#473) (#366)	$U = V = 0$, $U_1 = V_1$, $W_1 = W_2$, $W \cong 0$, $S_{11} = S_{22}$, $S_{13} = S_{23}$ (SB)

and S_{ij} the characteristics of these modes are determined and listed in the last column of Table 1. The (1, 1, 1) mode is a bending mode with small shear deformation and will be called a bending–shearing (BS) mode. Although the S_{13} of Mode (1, 1, 1) in Fig. 10a is small, it makes the classical plate theory cannot predict this frequency well. The (1, 1, 2) mode is a pure in-plane tension–compression (TC) mode, as shown later in Fig. 12. Mode (1, 1, 3) is a pure in-plane tension–tension (TT) mode. Because of the extension–extension deformation (i.e., $S_{11} = S_{22}$), the dynamical inertial stretching along the thickness direction caused by Poisson's effect results in a non-zero but small S_{33} in the 3D elasticity solution. This non-zero S_{33} cannot be predicted by this theory because Eq. (50) shows that the S_{33} in this theory only accounts for those caused by shear stresses S_{13} and S_{23}. If $u_3^{(i)} = w + \eta_1^{(i)} z + \eta_2^{(i)} z^2$ is assumed from the beginning in Eq. (1), this S_{33} can be also obtained [15]. Because there is no shear deformation in Modes (1, 1, 2) and (1, 1, 3), even the classical plate theory can predict these two frequencies well by post-processing the 3D elasticity equations after the reference-plane deformations u, v, and w are obtained from the plate theory. If u at $x = 0, a$ and v at $y = 0, b$ are fixed to zero, these two modes will be prevented from happening.

Mode (1, 1, 4) is a pure transverse S (shearing) mode, and Mode (1, 1, 5) is a transverse shear (see Fig. 2a and b) with small bending shear–bending (SB) mode. Mode (1, 1, 6) ($\overline{\omega}_{11,6} = 86.840$ in Ref. [14]) is missing because it is a thickness-stretching mode and it is excluded from the assumed displacement field shown in Eq. (1). Again, if $u_3^{(i)} = w + \eta_1^{(i)} z + \eta_2^{(i)} z^2$ is assumed from the beginning in Eq. (1), this mode would be also predicted [15]. Mode (1, 1, 7) is an shear–tension–compression (STC) mode with a major transverse shear accompanied by a small in-plane tension–compression deformation similar to Mode (1, 1, 2). Mode (1, 1, 8) is a shear–tension–tension (STT) mode with a major transverse shear accompanied by a small in-plane tension–tension deformation similar to Mode (1, 1, 3) (see Fig. 2). Mode (1, 1, 9) is an SB mode having transverse shears accompanied by a very small bending deformation. The stresses in Fig. 10 agree well with the 3D elasticity solutions (Fig. 2 in Ref. [14]). Eq. (50) shows that $S_{33}^{(i)}(z) \neq 0$ if $S_{13}^{(i)}(z) = S_{23}^{(i)}(z)$ and $\overline{m} = \overline{n}$, as

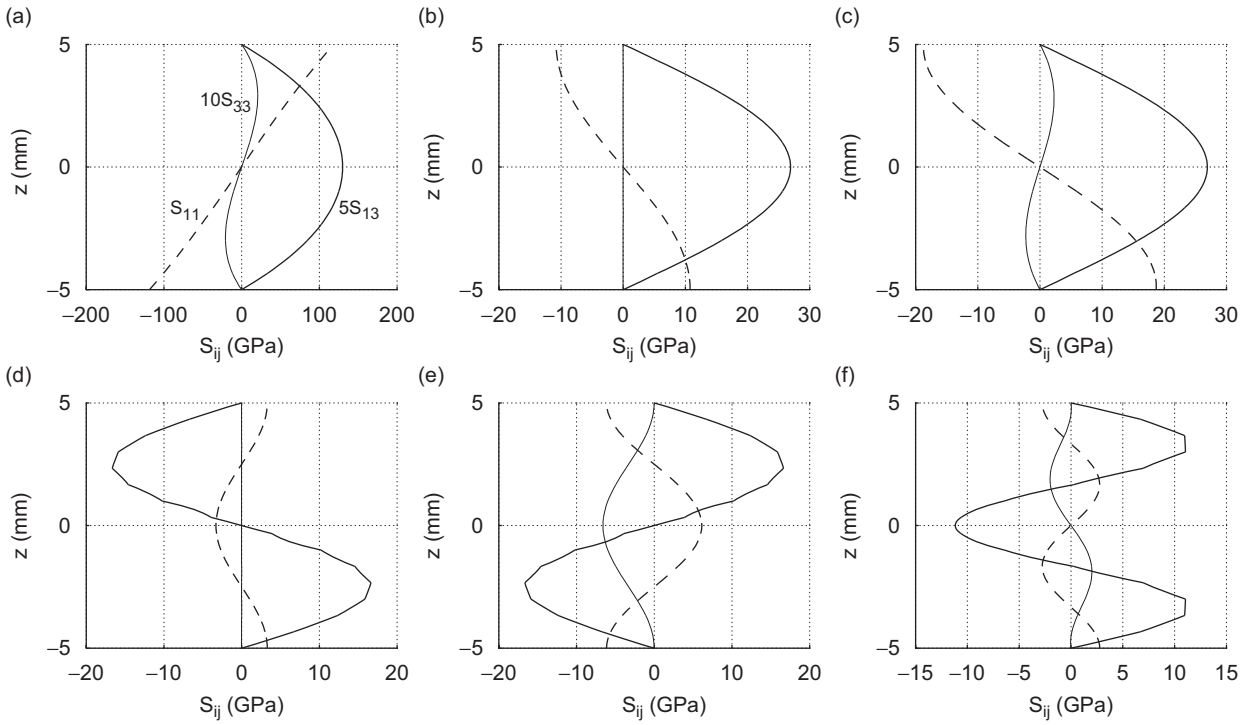

Fig. 10. The stress distributions of different modes: (a) Mode (1, 1, 1), (b) Mode (1, 1, 4), (c) Mode (1, 1, 5), (d) Mode (1, 1, 7), (e) Mode (1, 1, 8), and (f) Mode (1, 1, 9), where the solid, broken, and thin lines represent S_{13}, S_{11}, and S_{33}, respectively.

shown in Table 1 and Fig. 10a, c, e and f. In other words, the $S_{33}^{(i)}(z)$ is mainly due to Poisson's effect induced by the in-plane tension–tension deformation caused by shear strains, as shown in Fig. 2b. On the other hand, $S_{33}^{(i)}(z) = 0$ if $S_{13}^{(i)}(z) = -S_{23}^{(i)}(z)$ and $\overline{m} = \overline{n}$, as shown in Table 1 and Fig. 10b and d. However, if $u_3^{(i)} = w + \eta_1^{(i)} z + \eta_2^{(i)} z^2$ is assumed from the beginning in Eq. (1), this would result in a non-zero but small $S_{33}^{(i)}(z)$. All the results also confirm that S_{33} can be accurately predicted by post-processing results obtained from a 2D plate theory using the 3D elasticity equations.

The S_{13} curves in Fig. 10d–f become smooth when the number of layers is increased beyond 20, as shown in Fig. 11a. Fig. 11b shows that, although $\overline{\omega}_{11,9}$ is not accurate when only 3 layers are used, the predicted distributions of shear stresses are fairly accurate. However, the inaccurate S_{13} causes the integrated S_{33} to be non-zero on the top surface. Note that Fig. 11a and b have different scales because each is individually scaled to have its maximum $G_5^{[j]}$ to be one. If only the deformation dynamics of a plate's surfaces is the interest of analysis and/or testing, Mode (1, 1, 1) is the most important one. However, other thickness modes are important for accurate stress analysis and wave propagation study.

It is apparent that this method works well because the analytical reference-plane mode shapes of a simply supported isotropic (or orthotropic) plate are available and the reference-plane mode shapes are not sensitive to thickness vibrations even for thick plates. After a reference-plane mode shape is obtained using a 2D plate theory, the transverse normal stress $\sigma_{33}^{(i)}$ (and $\sigma_{13}^{(i)}$ and $\sigma_{23}^{(i)}$ if the classical plate theory is used) can be obtained by integrating Eq. (41), and all other strains and stresses can be obtained using the strain–displacement relations and constitutive equations (e.g., Eqs. (10) and (11)). Hence, the original 3D problem becomes 1D, as shown by Eqs. (45) and (48). However, for structures with no analytical reference-plane mode shapes, one needs to use a numerical method (e.g., the finite-element method) to obtain the reference-plane and thickness mode shapes simultaneously. Unfortunately, if a 2D plate theory does not have enough dofs for different thickness vibration modes (e.g., the classical, the first-order shear, and the third-order shear theories), the high-order modes shown in Figs. 10b–f cannot be obtained and restraint boundary conditions cannot be treated.

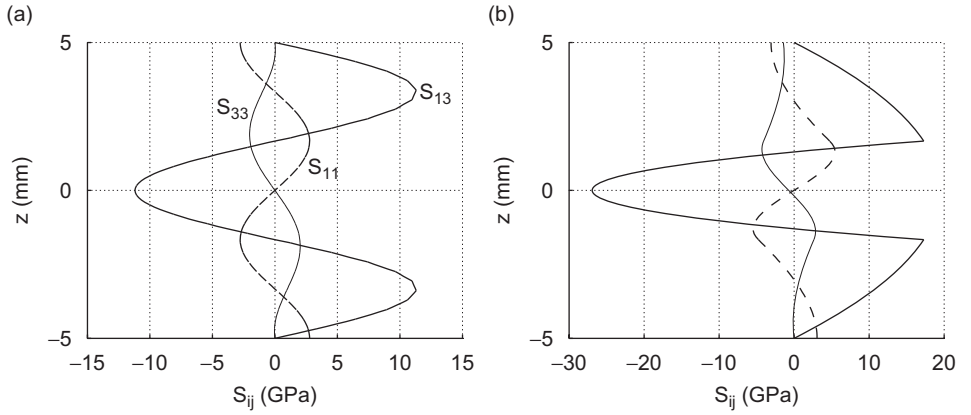

Fig. 11. The stress distributions of Mode (1, 1, 9) using: (a) 31 layers and (b) 3 layers, where the solid, broken, and thin lines represent S_{13}, S_{11}, and S_{33}, respectively.

4.3. Finite-element analysis and boundary restraint effects

Here we demonstrate that the SPE derived from the proposed SPT can accurately predict thickness modes and handle different boundary restraint effects. Moreover, the number of dofs of an SPE is adaptable and it can directly compute $\sigma_{13}^{(i)}$ and $\sigma_{23}^{(i)}$ without post-processing by integrating the 3D equilibrium equations.

It follows from Eqs. (42), (8), (10), (11), and (43) that, for a simply supported plate, the boundary conditions for using the SPT are

$$\begin{aligned} &v = w = w_y = \gamma_4^{[j]} = N_1 = M_1 = \overline{M}_1^{[j]} = 0 \quad \text{at } x = 0, a, \\ &u = w = w_x = \gamma_5^{[j]} = N_2 = M_2 = \overline{M}_2^{[j]} = 0 \quad \text{at } y = 0, b, \\ &\sigma_{13} = \sigma_{23} = 0 \quad \text{at } z = \pm h/2, \end{aligned} \tag{51}$$

where $j = 1, \ldots, J$ and

$$\{N_1, M_1, \overline{M}_1^{[j]}\} \equiv \sum_{i=1}^{I} \int_{z_i}^{z_{i+1}} \sigma_{11}^{(i)} \{1,\ z,\ z\delta_{ij} + g_{15}^{(i,j)}\}\, \mathrm{d}z,$$

$$\{N_2, M_2, \overline{M}_2^{[j]}\} \equiv \sum_{i=1}^{I} \int_{z_i}^{z_{i+1}} \sigma_{22}^{(i)} \{1,\ z,\ z\delta_{ij} + g_{24}^{(i,j)}\}\, \mathrm{d}z. \tag{52}$$

Note that the boundary conditions on σ_{13} and σ_{23} are automatically satisfied by the derived shear warping functions (see Eq. (4)). The boundary conditions $N_1 = M_1 = \overline{M}_1^{[j]} = 0$ at nodes on the boundaries $x = 0, a$ and $N_2 = M_2 = \overline{M}_2^{[j]} = 0$ at $y = 0, b$ are only to satisfy the boundary conditions $\sigma_{11}^{(i)} = 0$ at $x = 0, a$ and $\sigma_{22}^{(i)} = 0$ at $y = 0, b$ in an average sense. These boundary conditions can be enforced through the use of multiple-point constraints, but it is inconvenient for a displacement-based finite-element method because it involves u_x, u_y, v_x, v_y, w_{xx}, w_{yy}, γ_{4x}, γ_{4y}, γ_{5x}, and γ_{5y} that are not direct nodal dofs. If the stress boundary conditions are not appropriately implemented, accuracy may loose due to the free-edge effect. However, for a simply supported plate, σ_{11} is close to zero around $x = 0, a$ and σ_{22} is close to zero around $y = 0, b$ (see Eq. (47)), and hence the free-edge effect is not expected here.

Using 10×10 SPE elements the natural frequencies of the simply supported aluminum plate are obtained and also listed in Table 1. The frequencies are almost the same as those obtained from the analytical method shown in Section 4.2 using 3 and 11 layers, respectively. However, $\overline{\omega}_{11,1}$ is 1.5% higher because it is a bending-dominant mode and the polynomial shape functions used in the finite-element formulation makes the plate stiffer. When the number of elements increases to 15×15, $\overline{\omega}_{11,1}$, $\overline{\omega}_{11,2}$, and $\overline{\omega}_{11,3}$ reduce to 5.3368, 13.825, and

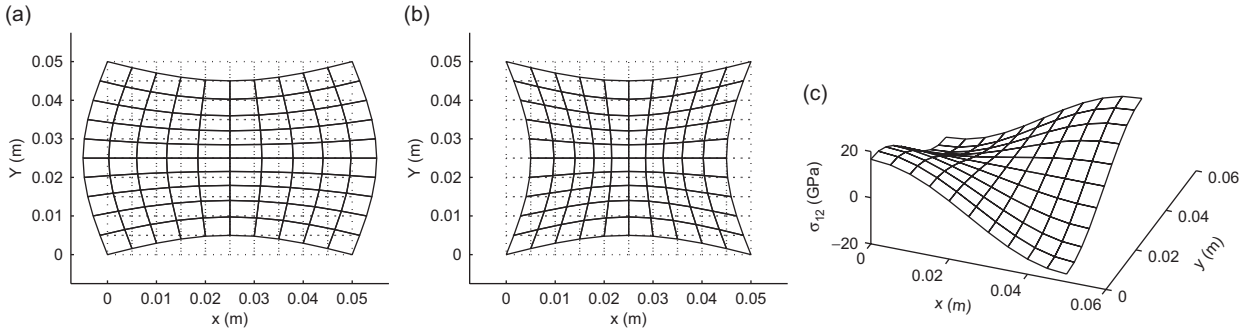

Fig. 12. Modes (1, 1, 2) and (1, 1, 3): (a) mode shape (1, 1, 2), (b) mode shape (1, 1, 3), and (c) σ_{12} of Mode (1, 1, 3).

23.316, but other $\overline{\omega}_{11,k}$ remain almost the same because they are not significantly coupled with the reference-plane bending. The distributions of S_{ij} are virtually the same as those in Fig. 10. With the use of 11 sublaminates and 11 layers, the total number of dofs is 2736 (after boundary conditions implemented). To reduce the number of dofs in modal analysis, one can use the mode shape of w of Mode (1, 1, 1) to reduce all the dofs of $w(x, y, t)$ into just one modal coordinate. This reduction does not cause any change of the mode shapes and natural frequencies shown in Table 1. This confirms again that these modes are not sensitive to the reference plane deformation shape. One can even use just one modal coordinate for each of $\gamma_4^{[j]}$ and $\gamma_5^{[j]}$ to reduce more dofs. With this reduction, the total number of dofs reduces from 2736 to 1785, and the obtained natural frequencies have a highest error only 0.6% at $\overline{\omega}_{11,9}$. Modes (1, 1, 2) and (1, 1, 3) are in-plane TC and TT modes, as shown in Fig. 12. It follows from the equation of $E_{12}^{(i)}$ in Eq. (46) and Table 1 that $E_{12} = S_{12} = 0$ for Mode (1, 1, 2) because $U = -V$, $\overline{m} = \overline{n}$, and $W = G_4^{(i)} = G_5^{(i)} = 0$. On the other hand, E_{12} and S_{12} are non-zero for Mode (1, 1, 3) and they have large in-plane shears around the four corners, as shown in Fig. 12c. As Table 1 shows, Mode (1, 1, 9) is actually the #473 (or #532 if 3 layers) mode in the finite-element analysis because there are many other low-frequency modes, including many thickness modes. With the use of $(m, n) = (1, 1)$ in the analytical method shown in Section 4.2 and other analytical methods in the literature, many modes with $W = 0$ (i.e., similar to Modes (1, 1, 2) and (1, 1, 3)) and having natural frequencies lower than $\overline{\omega}_{11,9}$ are missed. All the finite-element results validate the SPE.

Since it is common in high-temperature applications to employ a ceramic top layer as a thermal barrier to a metallic structure, we choose the constituent materials of the FGP for demonstration to be Aluminum (#1) and SiC (#2) having the following material properties:

$$E_1 = 70\,\text{GPa}, \quad \nu_1 = 0.3, \quad \rho_1 = 2702\,\text{kg/m}^3,$$

$$E_2 = 427\,\text{GPa}, \quad \nu_2 = 0.17, \quad \rho_2 = 3100\,\text{kg/m}^3. \tag{53}$$

Many actual applications of plates are constructed in a way similar to a cantilevered plate, as shown in Fig. 1. Moreover, setting up a cantilevered plate for experimental testing is much easier than setting up a simply supported plate. Unfortunately analytical mode shapes of a cantilevered plate do not exist. Hence, we will consider a 10 cm × 6 cm × 1 cm cantilevered plate to show the modeling capability of the sublamination plate element, the influences of boundary restraints, and the influences of material variation through the plate thickness on structural characteristics and the local stress distribution around boundaries. Using a shear-deformable 2D plate theory to analyze a cantilevered 3D solid different sets of boundary conditions may be used by different researchers because actual boundary conditions are affected by the clamping device, the clamping force, and the stiffness ratio of the plate and fixture materials. Here we assume the boundary conditions to be

$$u = v = w = w_x = w_y = u_1^{(1)}(0, y, -h/2, t) = u_1^{(I)}(0, y, h/2, t) = 0 \quad \text{at } x = 0,$$

$$\gamma_5^{(i)} = 0, \quad i = 1, \ldots, I \text{ (i.e., } \sigma_{13}^{(i)} = 0) \text{ at } x = a,$$

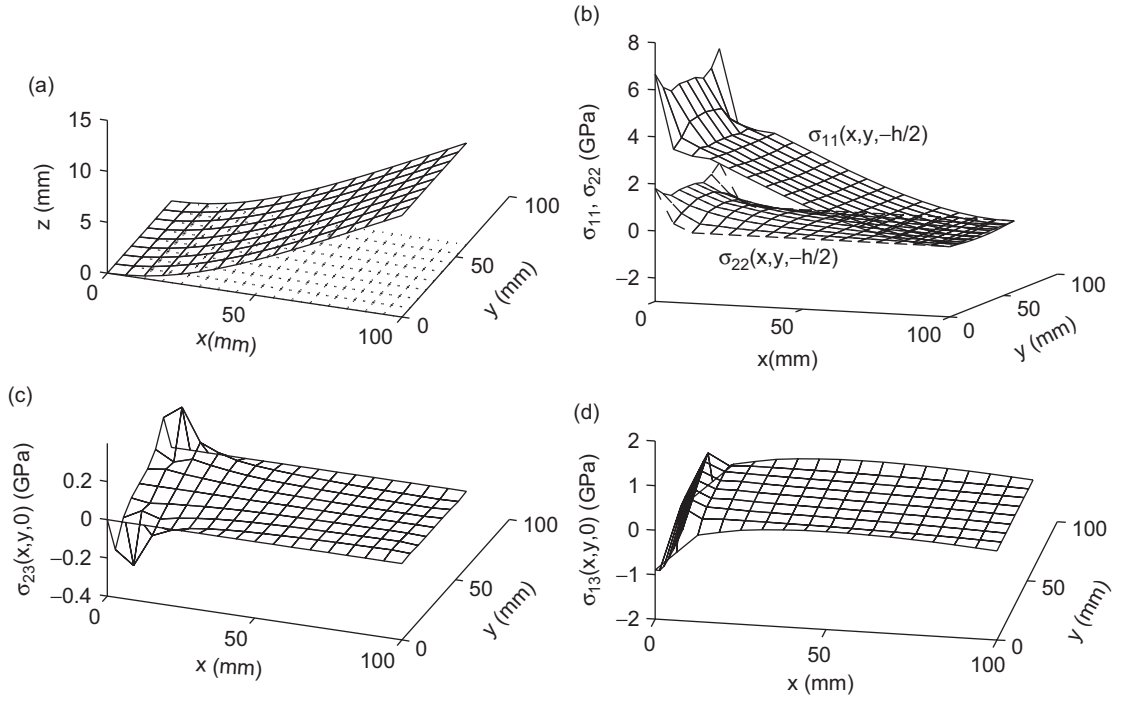

Fig. 13. The first bending mode: (a) reference-plane mode shape, (b) $\sigma_{11}(x, y, -h/2)$ (solid lines) and $\sigma_{22}(x, y, -h/2)$ (broken lines), (c) $\sigma_{13}(x, y, 0)$, and (d) $\sigma_{23}(x, y, 0)$.

$$\gamma_4^{(i)} = 0, \quad i = 1, \ldots, I \text{ (i.e., } \sigma_{23}^{(i)} = 0) \text{ at } y = 0, b. \tag{54}$$

The boundary conditions $u_1^{(1)}(0, y, -h/2, t) = u_1^{(I)}(0, y, h/2, t) = 0$ are implemented through multiple-point constraints on dofs of each node on the clamped edge. If the plate material is a uniform mixture of Aluminum and SiC with $V_1 = V_2 = 0.5$ through the whole thickness (i.e., a pure isotropic plate), Fig. 13 shows the first flexural mode shape of the reference plane and the xy-plane distributions of stresses. Because of the use of shear warping functions, all transverse shear stresses obtained from SPEs are continuous at any point (x, y, z) in the plate's 3D domain, as revealed by Eq. (37). However, just like any finite-element analysis of plates using 3D solid elements, σ_{11}, σ_{22}, and σ_{12} may not be continuous at nodes, and hence the averaged value is presented at each node. We note that the boundary restraint at the clamped end changes the thickness-direction distribution of σ_{13}, as shown in Fig. 14. The transition length can be used to quantify the boundary restraint effect. Note that the distribution of σ_{13} around $x = 0$ is similar to Fig. 7c due to the boundary restraints $u_1^{(1)}(0, y, -h/2) = u_1^{(I)}(0, y, h/2) = 0$. If the plate material is distributed according to Eq. (16) with $n = 1.0$ and $\bar{z}_1 = -h/2$, Fig. 15 shows the thickness-direction distributions of $\sigma_{13}(x, b/2, z)$ and $\sigma_{11}(x, b/2, z)$ at 16 different longitudinal locations. The distributions of σ_{13} and σ_{11} are asymmetric and the highest σ_{13} exists close to the top surface (i.e., the SiC-dominant area). If the plate material is distributed according to Eq. (16) with $n = 2.0$ and $\bar{z}_1 = -h/2$, Fig. 16 shows the thickness-direction distributions of $\sigma_{13}(x, b/2, z)$ and $\sigma_{11}(x, b/2, z)$ at 16 different longitudinal locations. We find that the upper part takes more share of stresses when the power index n increases. Note that $\sigma_{11}(x, b/2, 0)$ does not show significant bending–extension coupling. It may be due to the free boundary at $x = a$, $\sigma_{11}(a, y, z) = 0$ not being enforced, and/or the use of low-order, bilinear shape functions for $u(x, y)$ in the finite-element modeling, and this problem requires more studies. Fig. 17 shows the thickness-direction distributions of $\sigma_{13}(x, b/2, z)$ and $\sigma_{11}(x, b/2, z)$ of the second bending mode. Note that σ_{13} changes sign at a location different from that of σ_{11}. Figs. 14–17 show that, for an element away from boundaries and hence free from free-edge and boundary restraint effects, one can easily reduce its dofs without loss of accuracy by using specific ratios between $\gamma_4^{[j]}$ and $\gamma_5^{[j]}$, as demonstrated by Figs. 6 and 8.

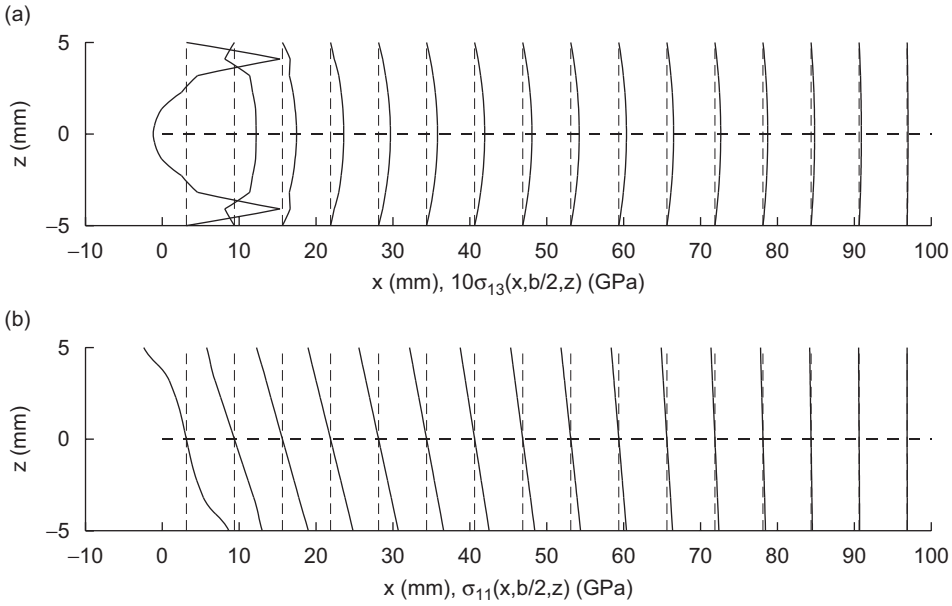

Fig. 14. The first bending mode with $V_1 = V_2 = 0.5$ through the thickness: (a) $\sigma_{13}(x, b/2, z)$ and (b) $\sigma_{11}(x, b/2, z)$.

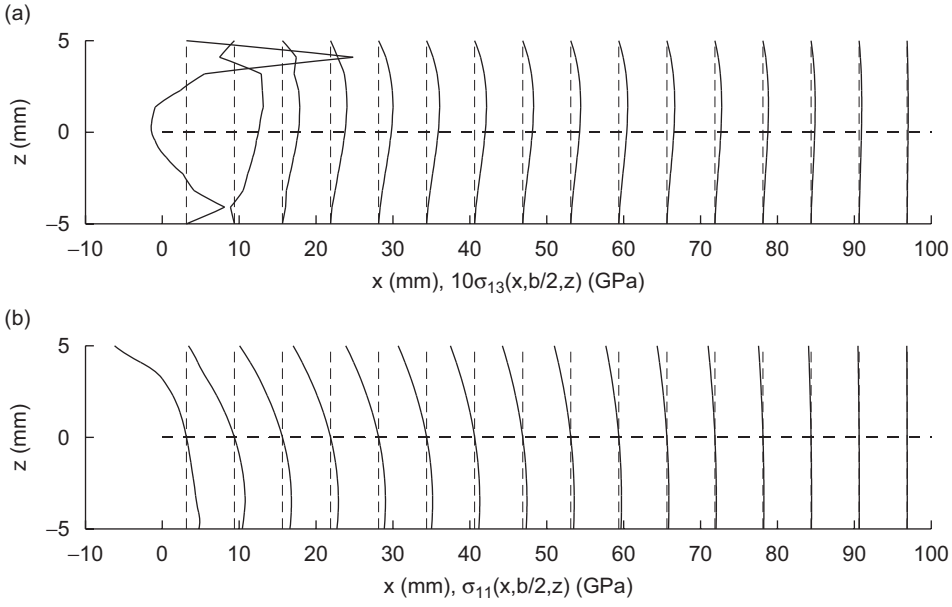

Fig. 15. The first bending mode with $n = 1.0$ and $\bar{z}_1 = -h/2$ in Eq. (16): (a) $\sigma_{13}(x, b/2, z)$ and (b) $\sigma_{11}(x, b/2, z)$.

Moreover, Figs. 16 and 17 show that, away from boundaries, the distribution profile of σ_{13} is the same and it is the one with all $\gamma_5^{[j]}$ having the same value (see Eq. (37)).

The first 12 modes of the cantilevered plate are the 1st B_y (796.38 Hz, Fig. 13a), 1st T_x (2779.4 Hz), 1st B_z (3830.9 Hz), 2nd B_y (4775.1 Hz), 2nd T_x (8950.1 Hz), 1st E_x (12,320 Hz), 3rd B_y (12,545 Hz), 2nd B_z (13,402 Hz), 1st B_y/1st B_x (14,438 Hz), 3rd T_x (16,934 Hz), 2nd B_y/1st B_x (19,605 Hz), and 4th B_y (23,427 Hz), where B_y means bending w.r.t. the y-axis, T_x means torsion w.r.t. the x-axis, B_z means bending w.r.t. the z-axis, E_x means extension along the x-axis, etc. Fig. 18 shows the second to tenth modes and natural

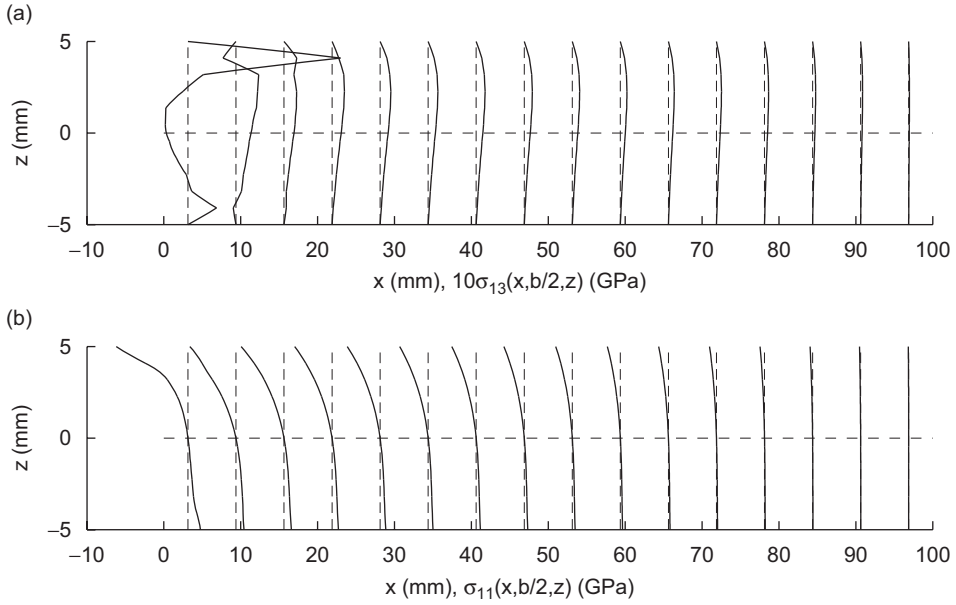

Fig. 16. The first bending mode with $n = 2.0$ and $\bar{z}_1 = -h/2$ in Eq. (16): (a) $\sigma_{13}(x, b/2, z)$ and (b) $\sigma_{11}(x, b/2, z)$.

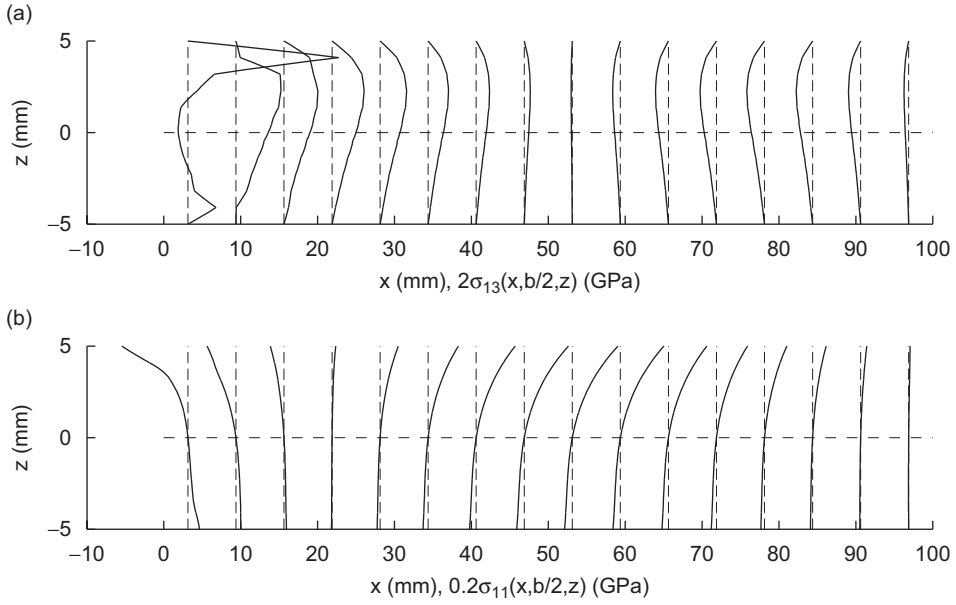

Fig. 17. The second bending mode with $n = 2.0$ and $\bar{z}_1 = -h/2$ in Eq. (16): (a) $\sigma_{13}(x, b/2, z)$ and (b) $\sigma_{11}(x, b/2, z)$.

frequencies when the bending mode shape is fixed to be the first bending mode by using one modal coordinate. We find that all of them are in-plane tension, compression, and/or shearing modes, and the transverse shears, if exist, have the same profile as that shown in Figs. 16a and 17a at locations away from boundaries. Because high-order transverse shears similar to those shown in Fig. 10d–f only exist at very high frequencies, they can be important for stress analysis and wave propagation studies under impulsive loading, but they would not have significant influences on the global surface dynamics of a plate, especially when the plate thickness becomes thin (e.g., $a/h,\ b/h > 10$).

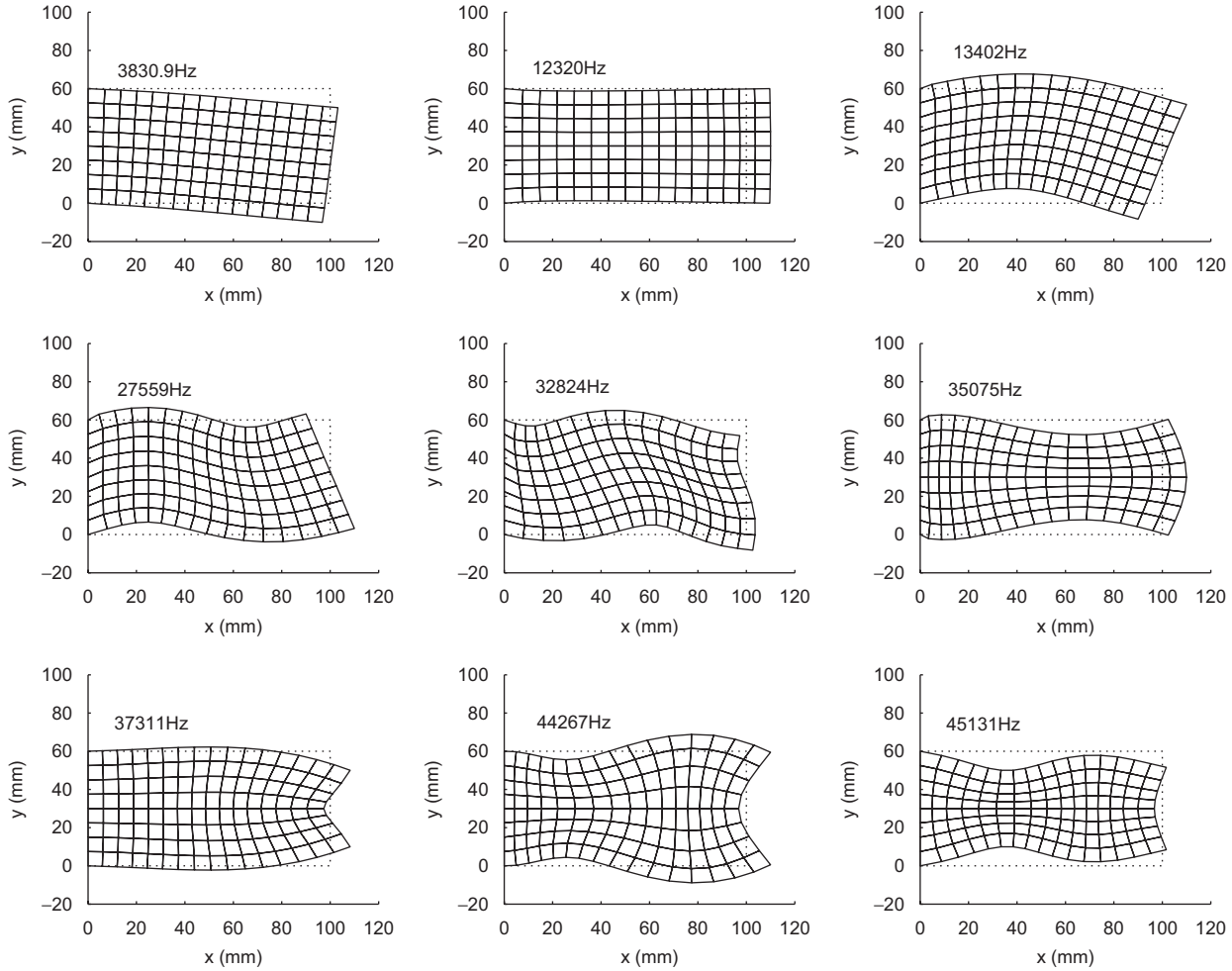

Fig. 18. The second to tenth modes under the first bending mode of the cantilevered plate with $n = 2.0$ and $\bar{z}_1 = -h/2$ in Eq. (16).

Any temperature variation through the plate thickness will affect the distribution of material properties and hence the dynamic characteristics of FGPs. To examine temperature effects one needs to use, for example, Eqs. (17) and (13) and consider the $\{\hat{F}^{[n]}\}$ in Eq. (23).

5. Concluding remarks

We presented a 2D sublamination theory of varying degrees of freedom (dof) for functionally graded plates that can account for layerwise higher-order transverse shear strains, continuity of interlaminar shear stresses, free shear-stress conditions on the bonding surfaces, and deformation-dependent shear warpings. The shear warping functions of a functionally graded plate are shown to depend on the detailed distribution of materials through the thickness, the vibration frequency, and boundary conditions. Moreover, a sublamination plate element of varying dofs is derived based on the plate theory and is numerically validated for performing analysis of complex stress states inside and around the boundaries of a functionally graded plate. The plate element can be used for detailed analysis of thick and thin plates with any boundary conditions. For quick analysis, one can use the theory with less dofs to obtain results equivalent to those from a 2D shear-deformable plate theory. For detailed analysis of stress states one can use the theory with more dofs to obtain results equivalent to those from 3D equilibrium equations.

Acknowledgments

The authors appreciate the support provided by the Structural Sciences Center of the Air Vehicles Directorate, US Air Force Research Laboratory, Wright Patterson AFB, Ohio.

References

[1] M.B. Bever, P.E. Duwez, Gradients in composite materials, *Materials Science and Engineering* 10 (1972) 1–8.
[2] T. Hirai, Functionally graded materials, in: R.J. Brook (Ed.), *Materials Science and Technology*, *Vol. 17B of Processing of Ceramics*, *Part 2*, VCH Verlags-gesellschaft mbH, Weinheim, Germany, 1996, pp. 292–341.
[3] S. Suresh, A. Mortensen, *Fundamentals of Functionally Graded Materials*, The Institute of Materials, IOM Communications Ltd., London, 1998.
[4] J. Aboudi, M.J. Pindera, S.M. Arnold, Higher-order theory for functionally graded materials, *Composites Part B-Engineering* 30 (1999) 777–832.
[5] A.J. Markworth, K.S. Ramesh, W.P. Parks Jr., Review modelling studies applied to functionally graded materials, *Journal of Materials Science* 30 (1995) 2183–2193.
[6] R. Hill, A self-consistent mechanics of composite materials, *Journal of the Mechanics and Physics of Solids* 13 (1965) 213–222.
[7] T. Reiter, G.J. Dvorak, Micromechanical modelling of functionally graded materials, in: X. Bahei-El-Din (Ed.), *IUTAM Symposium on Transformation Problems in Composite and Active Materials*, Kluwer Academic Publishers, London, 1997, pp. 173–184.
[8] T. Mori, K. Tanaka, Average stress in matrix and average elastic energy of materials with misfitting inclusions, *Acta Metallurgica* 21 (1973) 571–574.
[9] J. Aboudi, *Mechanics of Composite Materials—A Unified Micromechanical Approach*, Elsevier, Amsterdam, 1991.
[10] N.J. Pagano, Exact solutions for composite laminates in cylindrical bending, *Journal of Composite Materials* 3 (1969) 398–411.
[11] N.J. Pagano, Exact solutions for rectangular bidirectional composites and sandwich plates, *Journal of Composite Materials* 4 (1970) 20–34.
[12] S. Srinivas, A.K. Rao, C.V.J. Rao, Flexure of simply supported thick homogeneous and laminated rectangular plates, *ZAMM-Journal of Applied Mathematics and Mechanics* 49 (1969) 449–458.
[13] M. Savoia, J.N. Reddy, A variational approach to three-dimensional elasticity solutions of laminated composite plates, *Journal of Applied Mechanics* 59 (1992) 166–175.
[14] S.S. Vel, R.C. Batra, Three-dimensional exact solution for the vibration of functionally graded rectangular plates, *Journal of Sound and Vibration* 272 (2004) 703–730.
[15] P.F. Pai, A.N. Palazotto, A higher-order sandwich plate theory accounting for 3-D stresses, *International Journal of Solids and Structures* 38 (2001) 5045–5062.
[16] J.M. Whitney, *Structural Analysis of Laminated Anisotropic Plates*, Technomic Publishing Company, Inc., Lancaster, Pennsylvania, 1987.
[17] R.M. Jones, *Mechanics of Composite Materials*, second ed., Taylor & Francis, Inc., Philadelphia, PA, 1999.
[18] A.H. Nayfeh, P.F. Pai, *Linear and Nonlinear Structural Mechanics*, Wiley Interscience, New York, 2004.
[19] K. Washizu, *Variational Methods in Elasticity & Plasticity*, third ed., Pergamon Press Inc, New York, 1982.
[20] P.J. Davis, P. Rabinowitz, *Methods of Numerical Integration*, second ed., Academic Press, New York, 1984.
[21] P.F. Pai, A new look at shear correction factors and warping functions of anisotropic laminates, *International Journal of Solids and Structures* 32 (1995) 2295–2313.
[22] J.D. Renton, Generalized beam theory applied to shear stiffness, *International Journal of Solids and Structures* 27 (1991) 1955–1967.
[23] E.J. Barbero, J.N. Reddy, J.L. Teply, An accurate determination of stresses in thick laminates using a generalized plate theory, *International Journal for Numerical Methods in Engineering* 29 (1990) 1–14.
[24] A.K. Noor, W.S. Burton, Assessment of shear deformation theories for multilayered composite plates, *Applied Mechanics Reviews* 42 (1989) 1–13.